REGENERATION

Promotion of uterine reconstruction by a tissue-engineered uterus with biomimetic structure and extracellular matrix microenvironment

Long-mei Zhao[1,2]†, Lin-cui Da[1,3]†, Rui Wang[1], Long Wang[1], Yan-lin Jiang[1], Xiu-zhen Zhang[1], Ya-xing Li[1], Xiong-xin Lei[1], Yu-ting Song[1], Chen-yu Zou[1], Li-ping Huang[1], Wen-qian Zhang[1], Qing-yi Zhang[1], Qian-jin Li[1], Rong Nie[1], Yi Zhang[4], Yan Liang[4], Jesse Li-Ling[5], Hui-qi Xie[1,2]*

The recurrence rate for severe intrauterine adhesions is as high as 60%, and there is still lack of effective prevention and treatment. Inspired by the nature of uterus, we have developed a bilayer scaffold (ECM-SPS) with biomimetic heterogeneous features and extracellular matrix (ECM) microenvironment of the uterus. As proved by subtotal uterine reconstruction experiments, the mechanical and antiadhesion properties of the bilayer scaffold could meet the requirement for uterine repair. With the modification with tissue-specific cell–derived ECM, the ECM-SPS had the ECM microenvironment signatures of both the endometrium and myometrium and exhibited the property of inducing stem cell–directed differentiation. Furthermore, the ECM-SPS has recruited more endogenous stem cells to promote endometrial regeneration at the initial stage of repair, which was accompanied by more smooth muscle regeneration and a higher pregnancy rate. The reconstructed uterus could also sustain normal pregnancy and live birth. The ECM-SPS may thereby provide a potential treatment for women with severe intrauterine adhesions.

INTRODUCTION

With the increasing rate of uterus-related surgeries, intrauterine adhesions (IUAs) have also shown an uprising incidence and posed severe negative impacts on women's reproductivity and mental health. Currently, the standard treatment for IUA is transcervical resection of adhesion with adjuvant postoperative treatments such as intrauterine devices, uterine cavity balloons, estrogen, etc. However, the transcervical resection of adhesion is often accompanied by postoperative complications such as bleeding, perforation, and infection, and the recurrence rate of severe IUA is as high as 60% (*1*–*3*). Biomaterials such as sodium hyaluronate hydrogel and amniotic membrane are used to treat IUA because of their good biocompatibility but limited effectiveness in the treatment of severe IUA (*4*). There are still many problems, such as easy peeling, unsupportive, poor barrier effect, and poor tissue-induced regeneration (*5*). More effective methods of preventing and treating severe IUA are still to be developed.

Severe IUA is often accompanied by damage to the myometrium, resulting in reduced mechanical strength and collapse of the uterine wall, direct contact between the trauma surfaces to form adhesions, and an increased risk of uterine rupture in pregnancy (*6*, *7*). The myometrium not only plays an important role in the maintenance of uterine morphology and delivery but also provides a rich blood supply to the endometrium. Damage to the smooth muscle may lead to local ischemia and hypoxia in the endometrium, seriously affecting the outcome of IUA treatment (*7*). Therefore, it is important to provide proper mechanical support, establish an antiadhesion barrier, and promote regeneration of uterine smooth muscle in the treatment of severe IUA.

Biomimicking scaffolds with two distinct regions resembling stratified anatomical architecture may provide potential strategies for the repair of uterine with full-thickness defect. Small intestinal submucosa (SIS) is a bioderived material. In our preliminary studies, it was found that SIS was effective in promoting epithelial regeneration in the bladder, digestive tract, and skin (*8*–*10*). In addition, SIS is a potential antiadhesive barrier due to its heterogeneous surface structure, with a seamless structure on one side and a rough structure with interlocking fibers on the other (*11*). Hence, SIS was chosen as the endometrium of the tissue-engineered uterus (SPS).

In our previous study, polyurethane/SIS (PU/SIS), a hybrid composite with good compatibility and adjustable mechanical properties, was prepared (*12*, *13*). It was suitable for the repair of soft tissues with supportive and/or contractile properties such as bladder, esophagus, uterus, urethra, etc. On this basis, we have selected the PU/SIS composite with similar elastic modulus to the uterus as the myometrium of the SPS, which has excellent mechanical support properties and improved operational feasibility as an antiadhesion barrier for the treatment of IUA.

Loss of endometrial stem cells and substantial change in the tissue microenvironment are considered to be the main cause for pathological uterine regeneration (*14*). Analogous to the "seed and soil" theory, the function of endometrial stem cells is thought to be limited largely by the microenvironment of the repair site (*15*). Harnessing the endogenous stem cells and constructing a favorable microenvironment are thereby expected to achieve functional

[1]Department of Orthopedic Surgery and Orthopedic Research Institute, Laboratory of Stem Cell and Tissue Engineering, State Key Laboratory of Biotherapy, West China Hospital, Sichuan University, Chengdu, Sichuan 610041, China. [2]Frontier Medical Center, Tianfu Jincheng Laboratory, Chengdu, Sichuan 610212, China. [3]Reproductive Center of Fujian Maternity and Child Health Care Hospital, College of Clinical Medicine for Obstetrics & Gynecology and Pediatrics, Fujian Medical University, Fuzhou, Fujian 350001, China. [4]Research Core Facility of West China Hospital, Sichuan University, Chengdu, Sichuan 610041, China. [5]Center of Medical Genetics, West China Second University Hospital, Sichuan University, Chengdu, Sichuan 610041, China.
*Corresponding author. Email: xiehuiqi@scu.edu.cn
†These authors contributed equally to this work.

uterine regeneration (*14*, *15*). As an important component of the tissue microenvironment, extracellular matrix (ECM) contains intrinsic biochemical and mechanical cues that can regulate cellular phenotype and function in response to various physiological and pathological stimuli (*16*), particularly induction of chemotaxis of lineage-directed progenitor cells (*17*–*19*). In this study, we have modified the tissue-specific ECM on the surface of the SPS scaffold to build a bionic microenvironment for the induction of uterus functional regeneration. ECM usually comes from animal tissues or cells. Although the composition of the tissue-derived ECM is more similar to that of natural tissue, it usually faces greater risks of immune rejection and biosafety, as well as greater batch differences in practical applications (*20*). Because of the artificial control of the cell source, the culture conditions, and the preparation process, the cell-derived ECM is more stable and uniform, easier to process, and weakly immunogenic (*18*, *21*, *22*). However, current research on cell-derived ECM has mainly focused on mesenchymal stem cell (MSC)–derived ECM in vitro rather than the effect of tissue-specific cell–derived ECM material on regeneration in vivo (*22*–*25*). Whether tissue-specific cell–derived ECM can mimic the natural tissue ECM microenvironment and achieve functional regeneration has remained unclear. Here, the endometrial epithelial cells (ECs) and smooth muscle cells (SMCs) were selected as the functional cells to create a tissue-specific ECM on the surface of the SPS scaffold to verify the effect of ECM derived from functional cells on tissue functional regeneration.

In this study, we have developed a bilayer scaffold (ECM-SPS) with biomimetic heterogeneous features and ECM microenvironment. The bilayer structure has two distinct regions, which may meet the multiple needs for severe IUA repair, including antiadhesion barrier, mechanical support, and simultaneous regeneration of epithelium and smooth muscle. In addition, the tissue-specific cell–derived ECM on the scaffold surface also provided a mimetic tissue ECM microenvironment that may modulate host response, recruit endogenous stem cells, and induce stem cell–directed differentiation. The ECM-SPS thereby has a great potential for the treatment and prevention of severe IUA.

RESULTS

Preparation of bilayered SPS scaffold by biomimicking the uterine structure

The SIS and PU/SIS composites were prepared with a previously described method, and the PU/SIS composites with excellent mechanical strength was screened (*12*, *13*). The thicknesses of the SIS and PU/SIS layers were approximately 100 and 300 μm, which have matched with that of the endometrium and myometrium of rat uterus, respectively (Fig. 1A). Subsequently, the SIS and PU/SIS were stuck with PU emulsion to obtain an integrated bilayer scaffold that was denoted as SPS. The top surface of the SPS was dense and smooth, indicating that it can be used as a physical barrier to prevent adhesion, while the bottom surface was porous. The adhesive strength of the PU emulsions with various concentrations was assessed through a 180° peel test (Fig. 1B and fig. S1). When the PU emulsion concentration has reached 9%, a strong interface has formed between the two layers (fig. S1). Therefore, the 9% PU was used to prepare the SPS bilayer scaffold for the subsequent experiments.

Tissue-specific ECM modification of the bilayered SPS scaffold

As an important component of the microenvironment, the ECM can regulate various biological processes. In this study, we have simulated the uterine microenvironment by modifying the ECM of ECs and SMCs on the surface of SIS and PU/SIS, respectively. The ECM-modified SIS and PU/SIS were denoted as ECM_{EC}-SIS and ECM_{SMC}-PU/SIS, respectively. Then, the ECM_{EC}-SIS and ECM_{SMC}-PU/SIS were stuck with PU emulsion to obtain the ECM-SPS scaffold.

As shown in Fig. 2A, the ECs derived from the proliferation stage and the SMCs were inoculated onto the SIS and PU/SIS for 7 and 14 days, respectively, and had grown well and completely covered the scaffold surface (Fig. 2B and figs. S2 and S3). Thereafter, the decellularization was carried out by repeated freeze-thawing and Triton X-100 treatment. After decellularization, most of the cell components are removed (Fig. 2C). The residual DNA contents in the ECM_{EC}-SIS and ECM_{SMC}-PU/SIS were 22.68 ± 5.71 and 28.55 ± 2.76 ng/mg, respectively, both of which were below the internationally recognized criterion (50 ng/mg) (Fig. 2, D and E). Furthermore, the surface morphology, hydrophilicity, and elastic modulus of the scaffold have also changed considerably. It can be seen that the ECM derived from the ECs and SMCs have covered the surface of the SIS and PU/SIS, respectively (Fig. 2B and fig. S4A). Compared with the PU/SIS, the hydrophilicity of the ECM_{SMC}-PU/SIS has greatly improved (Fig. 2F). The elastic modulus of the ECM_{EC}-SIS was lower than that of SIS, while that of the ECM_{SMC}-PU/SIS was higher than the PU/SIS (Fig. 2G and fig. S4B).

To further assess the efficiency of the decellularization protocol, we also examined the major matrisome proteins and cytokines of the ECM. After ECM modification, the content of total protein and collagen increased significantly, while the content of glycosaminoglycan (GAGs) was comparable between the two groups (Fig. 2H). The expression of epithelial growth factor (EGF), heparin-binding growth factor (HGF), transforming growth factor–β (TGF-β), and platelet-derived growth factor–BB (PDGF-BB) have all become significantly higher in the ECM_{EC}-SIS compared with the SIS. By contrast, only the EGF and HGF were increased in ECM_{SMC}-PU/SIS, and the levels of TGF-β and PDGF-BB did not change significantly (Fig. 2I). The high contents of matrisome proteins and cytokines suggested that the scaffold has successfully been modified by the ECM and had high biological activity.

Proteomic analysis of the ECM signature of ECM_{EC}-SIS and ECM_{SMC}-PU/SIS

To better characterize the ECM signature of the ECM_{EC}-SIS and ECM_{SMC}-PU/SIS, we carried out a four-dimensional (4D) label-free proteomic analyses (Fig. 3A). The data shown in Fig. 3 were the results for ECM_{EC}-SIS and ECM_{SMC}-PU/SIS (data S1 and S2), which had excluded the SIS-derived proteins.

In total, 2761 and 1520 proteins have been identified for the ECM_{EC}-SIS and ECM_{SMC}-PU/SIS, respectively, including 1055 in common (Fig. 3B). An ECM-specific categorization database, MatrisomeDB 2.0, was used to analyze the ECM matrisome protein and ECM-associated proteins. The matrisome signatures of the ECM_{EC}-SIS and ECM_{SMC}-PU/SIS differ considerably (fig. S5A) but were similar to those of endometrium and myometrium, respectively (Fig. 3, C and D, and fig. S5) (*26*–*30*). For example, ECM_{EC}-SIS contained proteins related to endometrial function, such as

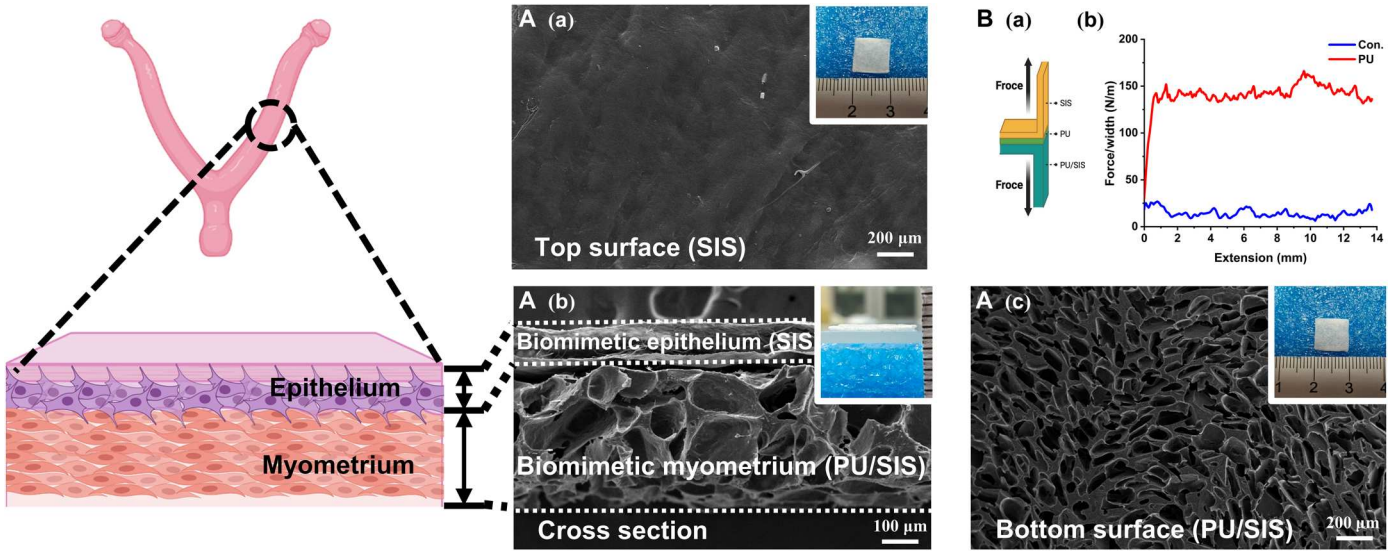

Fig. 1. Preparation of the bilayered SPS composites biomimicking the uterine structure. (**A**) Scanning electron microscope (SEM) images of the top [(Aa) scale bar, 200 μm)] cross-sectional [(Ab) scale bar, 100 μm], and bottom [(Ac) scale bar, 200 μm] micromorphology of the SPS composites. Inside the white frame is the macroscopic morphology of the SPS. (**B**) Schematic of the 180° peel test (Ba). The force-extension curves of the bilayered SPS composites (Bb).

collagen-3 (COL3), COL5, and lumican (LUM), while a large number of proteins related to myometrial function were detected in ECM_{SMC}-PU/SIS, such as COL1, COL6, fibronectin (FN), and fibrinolin-1 (FBN1) (Fig. 3E). A recent study suggested that COL3 could bind with TGF-β in a dose-dependent manner to attenuate TGF-β signaling, showing a significant inhibitory effect on tissue fibrosis (*31*). This suggested that the high abundance of COL3 in ECM_{EC}-SIS might provide a better tissue microenvironment for endometrial repair and inhibit endometrial fibrosis. Second, the high abundance of key proteins of TGF-β signaling pathway such as CREB binding protein (CREBBP), latent TGF-β–binding protein 1 (LTBP1), and cartilage oligomeric matrix protein (COMP) were detected in ECM_{SMC}-PU/SIS, which contribute to smooth muscle regeneration and differentiation (Fig. 3E). Subsequently, we conducted enrichment analysis on differentially expressed proteins. The results of gene ontology enrichment analysis showed that these differential proteins were enriched in terms such as cell adhesion, proliferation, migration, stem cell differentiation, wound healing, etc. (Fig. 3F). In Gene Set Enrichment Analysis, we also found that the Mesenchymal-epithelial transition (MET) signaling pathway related to epithelial regeneration and differentiation was significantly up-regulated in ECM_{EC}-SIS, while the TGF-β signaling pathway related to smooth muscle regeneration and differentiation was significantly up-regulated in ECM_{SMC}-PU/SIS (Fig. 3G). These results suggested that epithelial and SMC-derived ECM has great potential advantages in inducing epithelial and smooth muscle regeneration.

Behaviors of the MSCs as regulated by ECM-SPS in vitro

MSCs persist in the endometrium to maintain the cyclical regeneration of the uterus (*14*, *32*), especially the leucine-rich G protein–coupled receptor 5 (Lgr5)–positive MSCs that are responsible for the development, maintenance, and regeneration of multiple ECs and the development of uterine glands (*33*). Loss or impairment of the MSCs may lead to scar regeneration and serious impairment of uterine function. How to recruit and induce MSCs to differentiate into functional cells is the key to inhibit the occurrence and development of IUA (*34*). In this study, the proteomic analyses revealed that the ECM proteins of ECM_{EC}-SIS and ECM_{SMC}-PU/SIS have participated in a variety of biological processes, including cell adhesion, proliferation, migration, differentiation, and wound healing, and show a potential role in inducing stem cell differentiation. Therefore, we have assessed the effect of ECM_{EC}-SIS and ECM_{SMC}-PU/SIS on the biological behaviors of the Lgr5-positive MSCs (fig. S6, A and B) to explore their roles and mechanism in inducing uterine functional regeneration.

Both ECM_{EC}-SIS and ECM_{SMC}-PU/SIS have exhibited good cytocompatibility. After 3 days culture of MSCs on ECM_{EC}-SIS and ECM_{SMC}-PU/SIS, the MSCs maintained excellent viability. Fewer dead cells (red) could be observed, and the live/dead ratio was not significant (fig. S6C). Furthermore, the cytoskeleton staining showed that the MSCs exhibited spindle-like shape and arranged in a tendency on the ECM_{SMC}-PU/SIS, while the MSCs were flatted and irregular on the PU/SIS (fig. S6, D and E). We found that more MSCs have attached to the surface of the ECM_{SMC}-PU/SIS, with a rate higher than that of the PU/SIS (Fig. 4, A and B). We speculated that this may be attributed to the increase in cell adhesion sites on the surface of the PU/SIS after ECM modification. Furthermore, the cell-derived ECM provides a naturally occurring substrate for cell viability and growth. The ECM_{EC}-SIS and ECM_{SMC}-PU/SIS exhibited higher cell proliferation rate than SIS and PU/SIS, respectively (Fig. 4C).

To investigate the differentiation of the MSCs in specific ECM-modified scaffolds, we cultured the MSCs on the SIS, ECM_{EC}-SIS, PU/SIS, and ECM_{SMC}-PU/SIS, respectively. After 3 and 7 days of culture, the gene relative expression of ECs-specific markers, *E-Cadherin* and *CK18*, in the ECM_{EC}-SIS was significantly higher compared with the SIS (Fig. 4D). Similarly, a significant number of E-Cadherin and CK18-positive cells were found on the ECM_{EC}-SIS but not the SIS (Fig. 4E). As for ECM_{SMC}-PU/SIS,

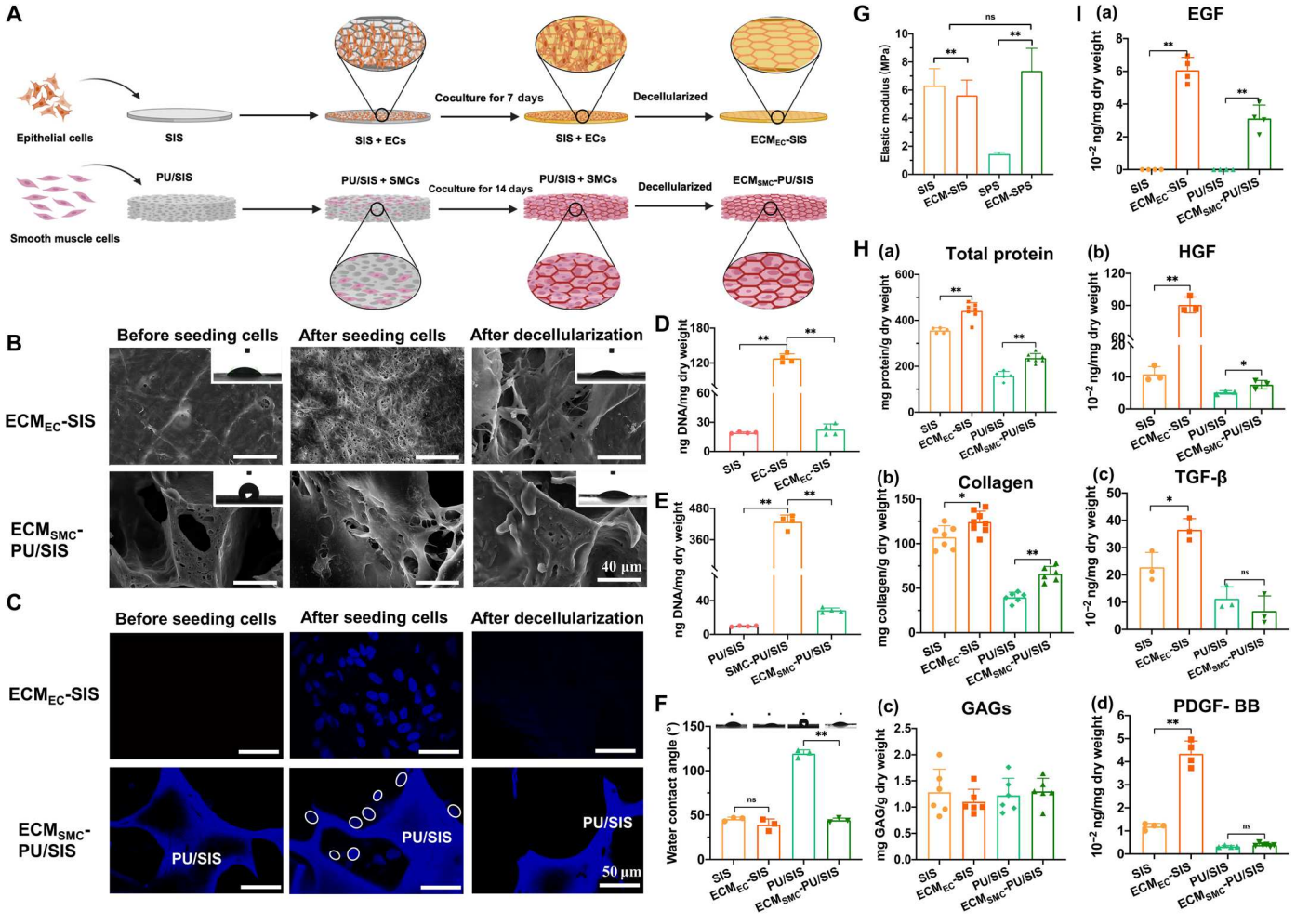

Fig. 2. Preparation and evaluation of the ECM-modified scaffold. (**A**) The procedures for the preparation of the ECM_{EC}-SIS and ECM_{SMC}-PU/SIS scaffolds. (**B**) The morphology and microstructure of the scaffold before and after the decellularization by SEM. Scale bars, 40 μm. Inside the white frame is the water contact angle. (**C**) 4′,6-diamidino-2-phenylindole (DAPI) staining of the scaffold before and after the decellularization. Scale bar, 50 μm. The circles marked the nucleus. (**D**) The residual DNA content of the ECM_{EC}-SIS before and after the decellularization ($n = 4$ independent samples, $^{**}P < 0.01$). (**E**) The residual DNA content of the ECM_{SMC}-PU/SIS before and after the decellularization ($n = 4$ independent samples, $^{**}P < 0.01$). (**F**) The water contact angle of the ECM_{EC}-SIS and ECM_{SMC}-PU/SIS scaffolds ($n = 3$, $^{**}P < 0.01$). ns, not significant. (**G**) The elastic modulus of the ECM_{EC}-SIS and ECM_{SMC}-PU/SIS scaffolds as detected by an atomic force microscope. (**H**) Quantification of total proteins ($n = 5$ independent samples, $^{**}P < 0.01$), collagen ($n = 6$ independent samples, $^{*}P < 0.05$ and $^{**}P < 0.01$), and GAGs ($n = 6$ independent samples, ns) in the ECM_{EC}-SIS and ECM_{SMC}-PU/SIS scaffolds. (**I**) The content of EGF ($n = 4$ independent samples, $^{**}P < 0.01$), HGF ($n = 3$ independent samples, $^{**}P < 0.01$ and $^{*}P < 0.05$), TGF-β ($n = 3$ independent samples, $^{*}P < 0.05$ and ns), and PDGF-BB ($n = 4$ independent samples, $^{**}P < 0.01$ and ns) in the ECM_{EC}-SIS and ECM_{SMC}-PU/SIS scaffolds as determined by enzyme-linked immunosorbent assay (ELISA) analysis.

the gene relative expression of α-*SMA* was significantly higher than that in the PU/SIS, but the gene relative expression of *myosin*, a marker of smooth muscle maturation, did not differ between the ECM_{SMC}-PU/SIS and PU/SIS (Fig. 4F). Furthermore, immunofluorescence results also showed that the expression of α–smooth muscle actin (α-SMA) was higher in the ECM_{SMC}-PU/SIS than PU/SIS after 21 days of culture, while myosin was weakly expressed in both groups (Fig. 4G). These demonstrated that both the ECM_{EC}-SIS and ECM_{SMC}-PU/SIS could promote the differentiation of the MSCs into ECs and SMCs, but the ECM_{SMC}-PU/SIS has lacked the cues for promoting smooth muscle maturation. The above results have indicated that the cell-derived ECM can simulate the microenvironment of tissue ECM to induce the MSC lineage-directional differentiation.

Performance of the SPS and ECM-SPS in vivo

Hemocompatibility is a critical indicator for the biocompatibility of biomaterials. Before implantation, the hemocompatibility of the SPS and ECM-SPS was assessed with a hemolysis assay, and the results showed that neither has triggered a hemolysis reaction (fig. S7). Subsequently, the SPS and ECM-SPS scaffolds were implanted into the rats′ back muscles to explore their capability for cellularization, vascularization, and immunoregulatory effect. As shown by hematoxylin and eosin (H&E) and DAPI staining, a large number of tissue cells have infiltrated into both scaffolds 4 weeks after the surgery. However, it was evident that the ECM-SPS has integrated better with the native tissues, while the SPS had a slight separation from the surrounding tissue (Fig. 5, A and B). It is unclear whether this gap was caused by external forces during tissue sectioning or

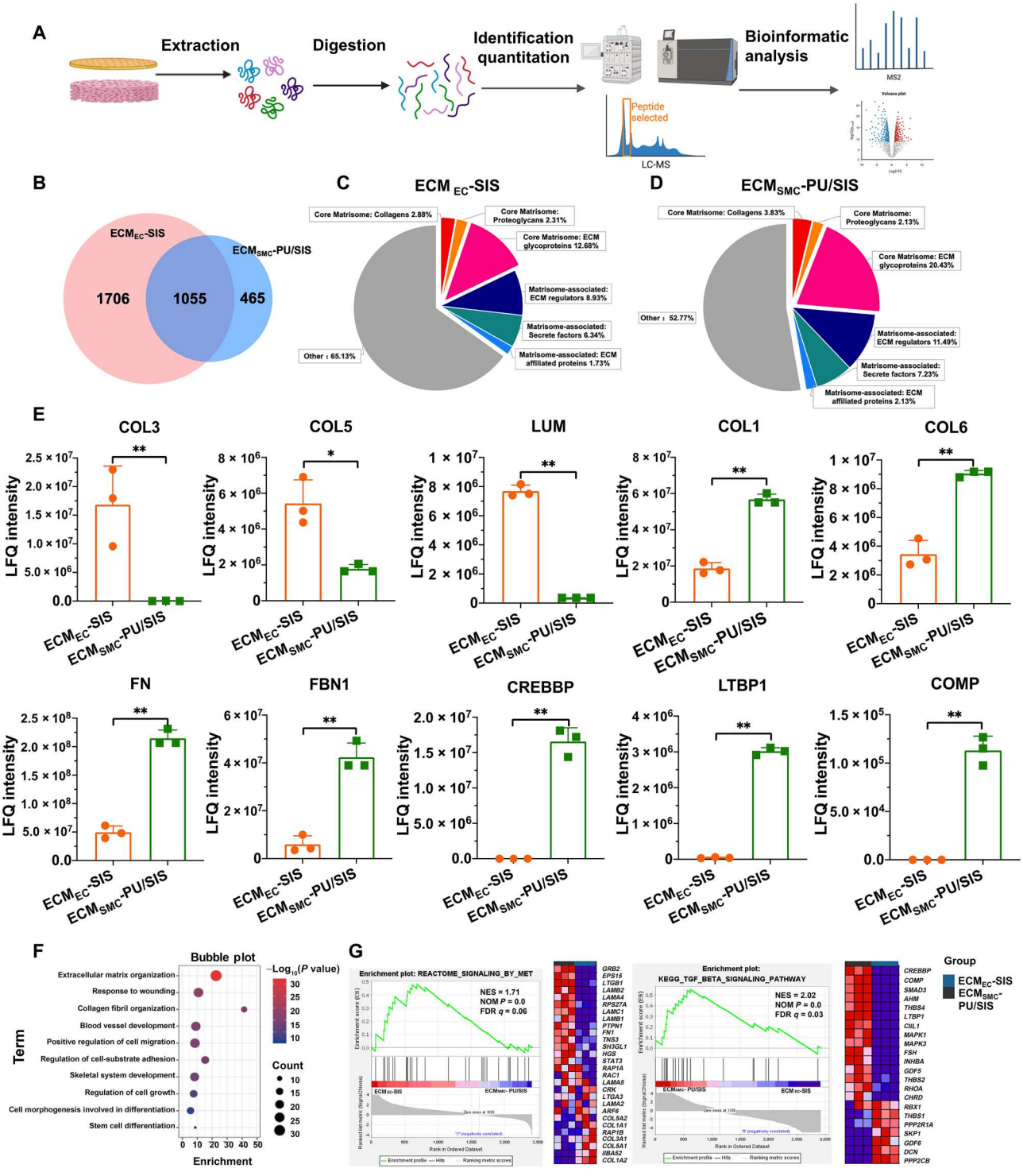

Fig. 3. Quantitative proteomic analysis of the ECM$_{EC}$-SIS and ECM$_{SMC}$-PU/SIS. (**A**) Scheme of dECM protein digestion of the ECM$_{EC}$-SIS and ECM$_{SMC}$-PU/SIS and subsequent mass spectrometry characterization. LC-MS, liquid chromatography–mass spectrometry. (**B**) Venn diagram of the protein numbers for the ECM$_{EC}$-SIS and ECM$_{SMC}$-PU/SIS. (**C** and **D**) Matrisome signatures of the ECM$_{EC}$-SIS (C) and ECM$_{SMC}$-PU/SIS (D). Pie chart represents the distribution of proteins by percentage of total number for each matrisome protein subcategory. (**E**) The label free quantified (LFQ) expression of partial ECM proteins in ECM$_{EC}$-SIS and ECM$_{SMC}$-PU/SIS (n = 3 independent samples, *P < 0.05 and **P < 0.01). (**F**) Gene ontology term enrichment analysis of the biological processes. (**G**) Gene set enrichment analysis of ECM$_{EC}$-SIS and ECM$_{SMC}$-PU/SIS [|normalized enrichment score| (|NES|) > 1, nominal (NOM) P < 0.05, and false discovery rate (FDR) q < 0.25 were set as the significant thresholds].

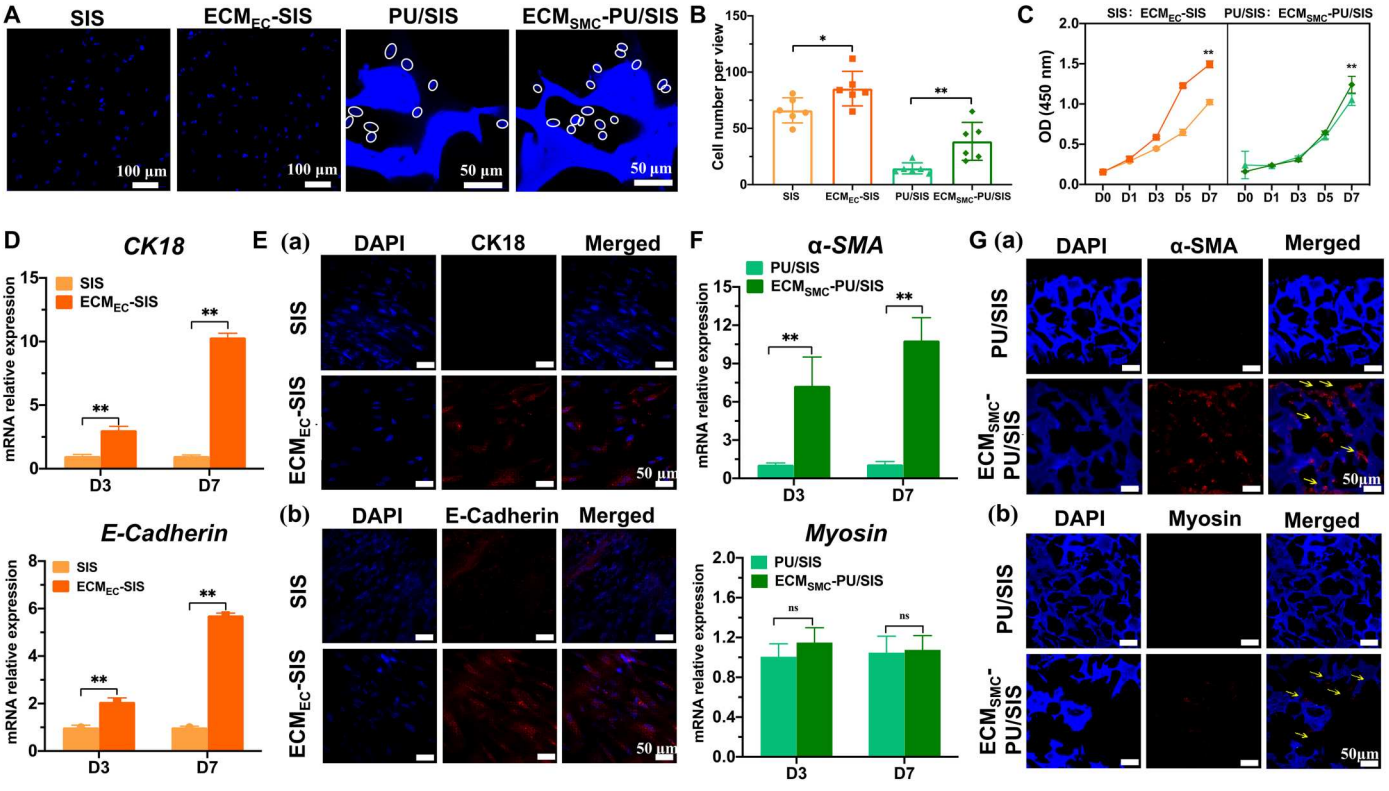

Fig. 4. Behaviors of the MSCs as regulated by the ECM_{EC}-SIS and ECM_{SMC}-PU/SIS in vitro. (**A**) The numbers of cells attached to the ECM_{EC}-SIS (scale bar, 100 μm) and ECM_{SMC}-PU/SIS were determined by DAPI staining (scale bar, 50 μm). The circles have marked the nuclei. (**B**) Quantification of cell number attached to the scaffold ($n = 6$ independent samples, $^{*}P < 0.05$ and $^{**}P < 0.01$). (**C**) The proliferation curve of the MSCs cultured with extracts of the ECM_{EC}-SIS and ECM_{SMC}-PU/SIS as evaluated by the CCK-8 assay ($n = 5$ independent samples, $^{**}P < 0.01$). (**D**) Relative mRNA expression of *CK18* and *E-Cadherin* in the MSCs cultured with the SIS or ECM_{EC}-SIS ($n = 3$ independent samples, $^{**}P < 0.01$). (**E**) Immunofluorescence staining of CK18 (Ea) and E-Cadherin (Eb) in the MSCs cultured with the SIS or ECM_{EC}-SIS. Scale bars, 50 μm. (**F**) Relative mRNA expression of α-*SMA* and *myosin* in the MSCs with the PU/SIS or ECM_{SMC}-PU/SIS ($n = 3$ independent samples, $^{**}P < 0.01$ and ns). (**G**) Immunofluorescence staining of α-SMA (Ga) and myosin (Gb) in the MSCs with the PU/SIS or ECM_{SMC}-PU/SIS. Scale bars, 50 μm.

absence of tissue cell infiltration, but it has indicated that the surface of the ECM-SPS was better for cell adhesion and that the cell-derived ECMs have enhanced host response and integration in comparison with synthetic materials, which is in keeping with the results of cell adhesion assays in vitro. As a result, the number of cells in the ECM-SPS was significantly greater than that in the SPS (Fig. 5C).

In addition, as evidenced by immunostaining for CD31, there was a higher vascular density in the ECM-SPS group. Notably, modification of SMC-derived ECM significantly enhanced the proangiogenic effect of the scaffold. As shown in Fig. 5, D and E, the vascular density in the ECM-PU/SIS layer was significantly higher than that in the PU/SIS layer. It suggested that the SMC-derived ECM constructs a bionic microenvironment that is more conducive to angiogenesis.

As a foreign body, the scaffold can often trigger an immune response and local inflammatory cell infiltration following the implantation. Previous studies have shown that the macrophages play an important role in tissue regeneration and usually have two phenotypes, i.e., CD86-positive M1 macrophages and CD206-positive M2 macrophages. As shown by CD86 and CD206 immunofluorescence staining, there were more M1 macrophages in the SPS group, whereas the numbers of M2 macrophages were similar between the two groups (Fig. 5, F to I). The above results have suggested superior cellularization, vascularization, and immunomodulation capacity of the ECM-SPS to the SPS.

Evaluation of the uterine regeneration efficacy in vivo

To assess their potential for treating severe IUA, we treated rats undergoing subtotal semicircular excision of uterine horns with the SPS and ECM-SPS scaffolds. The surgical procedures are shown in Fig. 6A. Rodent uterus has an inherent regenerative potential, and small defects can self-heal without treatment. Therefore, the small defects created in most instances may not be clinically meaningful. To determine the critical size for the defect, we have created uterine defects with sizes of 1.5 × 0.5, 1.0 × 0.5, and 0.5 × 0.5 cm and observed their self-healing rates in the natural state (fig. S8). As shown, when the defect length is 0.5 cm, the edges of all uteri could heal by themselves. At a defect length of 1.0 cm, the healing rate was 66.67%. The self-healed uteri were significantly narrower, and their cavity size was significantly smaller than that of normal uteri. When the defect was 1.5 cm in length, the healing rate was only 16.67%. Therefore, a defect size of 1.5 × 0.5 cm was selected for subsequent experiments.

The animals were euthanized at 4, 8, and 12 weeks postoperatively. As shown in fig. S9, there were no obvious adhesion and reproductive tract abnormalities. The SPS and ECM-SPS scaffold exhibited excellent mechanical properties and maintained a

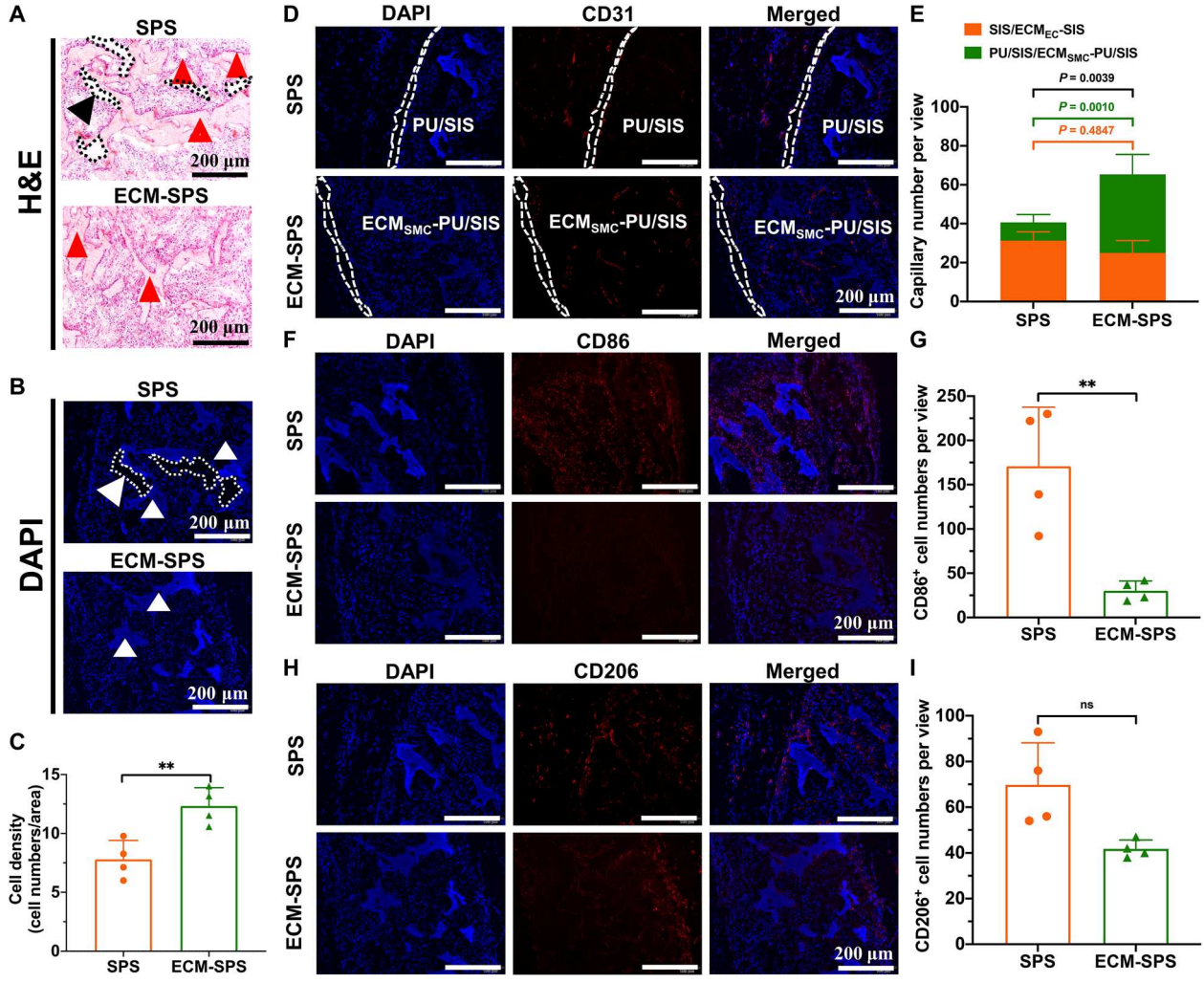

Fig. 5. In vivo cellularization, vascularization and immunogenic properties of the SPS and ECM-SPS 4 weeks after the surgery. (**A**) H&E and (**B**) DAPI staining of the cross sections showing cell infiltration within the SPS and ECM-SPS. The arrowheads indicated the scaffolds, and the dotted lines marked the blank area between the SPS and surrounding tissue. Scale bars, 200 μm. (**C**) Quantification of cell numbers within the SPS and ECM-SPS (n = 4 independent samples, $^{**}P < 0.01$ and ns). (**D**) CD31 immunofluorescent staining showing vascularization within the scaffolds. The SIS layer and ECM_{EC}-SIS layer were marked with the dashed lines. Scale bars, 200 μm. (**E**) Quantification of capillaries number within the SPS and ECM-SPS (n = 4 independent samples, $^{*}P < 0.05$, $^{**}P < 0.01$, and ns; orange represents SIS group or ECM_{EC}-SIS group, and green represents PU/SIS group or ECM_{SMC}-PU/SIS group). (**F**) M1 macrophages as detected by CD86 immunofluorescence staining. Scale bars, 200 μm. (**G**) Quantification of CD86 positive cell numbers within the SPS and ECM-SPS (n = 4 independent samples, $^{**}P < 0.01$). (**H**) M2 macrophages as detected by CD206 immunofluorescence staining. Scale bars, 200 μm. (**I**) Quantification of CD206-positive cell numbers within the SPS and ECM-SPS (n = 4 independent samples, ns).

normal uterine cavity without stenosis or adhesions, whereas uterine cavity effusion and stenosis were observed in the excision-only controls. It proved that the mechanical and antiadhesion properties of the SPS and ECM-SPS scaffold could meet the requirement for uterus scaffold. Subsequently, only histological data for the SPS and ECM-SPS groups are shown.

The repairing effect of the SPS and ECM-SPS was further evaluated by histological analysis. Tissue cross sections were subjected to H&E and Masson's trichrome staining to show the endometrial regeneration and remodeling at 4, 8, and 12 weeks postoperatively. By H&E staining, bilayer structure of the SPS and ECM-SPS was clearly shown in the nascent region at 4 and 8 weeks postoperatively. As shown in Fig. 6B, most epithelium has regenerated along the SIS or ECM_{EC}-SIS (indicated by the pentastars), while more smooth muscle has regenerated around with the PU/SIS or ECM_{SMC}-PU/SIS (indicated by the trigons). This suggested that the bilayer scaffold with two distinct regions could better fulfill the requirement for endometrial epithelial and smooth muscle regeneration and attain simultaneous regeneration of both the endometrium and myometrium.

Endometrium affects the receptivity of the uterus. A thin endometrium may hamper embryonic implantation (*35*). As the thickness of the endometrium changes cyclically in response to the levels of estrogen and progesterone, we have collected the samples in estrus to evaluate the regeneration of the endometrium. At the initial stage of repair, the endometrial regeneration in the ECM-SPS group was significantly better than the SPS group. At 4 weeks postoperatively, the ECM-SPS group showed significant

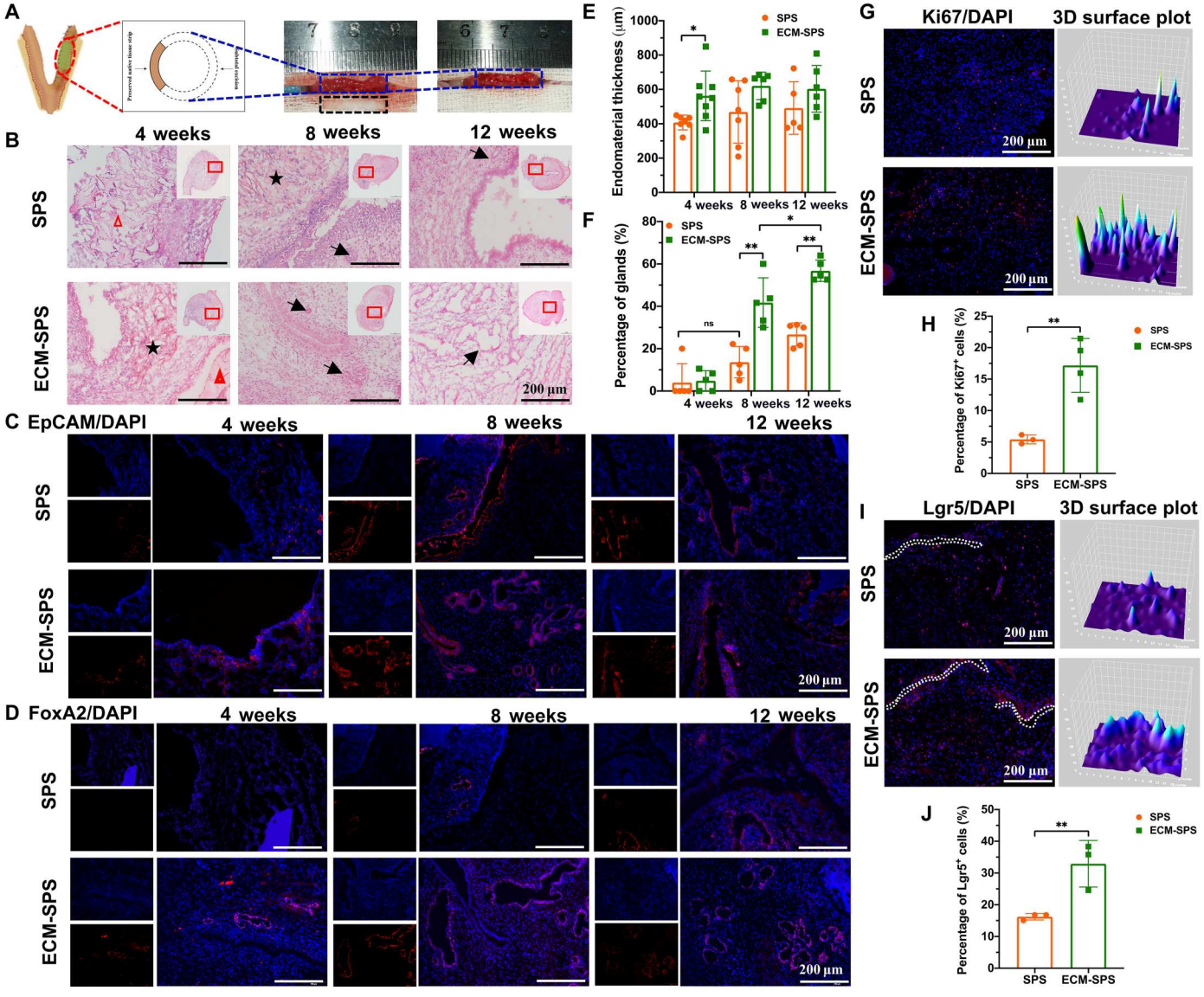

Fig. 6. The endometrial effects of various interventions on the epithelium and gland regeneration. (**A**) Schematic drawing of the subtotal uterine excision (blue dashed box) and scaffold (black dashed box) implantation procedures. (**B**) H&E staining of reconstructed uterine segments. Inserts are the corresponding gross views, and the magnified regions are marked with red squares. The black arrows indicated the glands. The pentagram indicated the SIS or ECM_{EC}-SIS. The triangle represented the PU/SIS or ECM_{SMC}-PU/SIS. Scale bars, 200 μm. (**C**) Immunostaining of EpCAM for endometrium regeneration in the reconstructed uterine segments. Scale bars, 200 μm. (**D**) Immunostaining of FoxA2 for endometrium glands in the reconstructed uterine segments. Scale bars, 200 μm. (**E**) Statistical analysis of average endometrial thickness (n = 5 independent samples, $^{*}P < 0.05$). (**F**) Statistical analysis of the percentage of glands (n = 5 independent samples, $^{*}P < 0.05$, $^{**}P < 0.01$, and ns). (**G**) Immunostaining of Ki67 for cell proliferation 7 days after the implantation. Scale bars, 200 μm. The 3D surface plot has represented the distribution and fluorescence intensity of the Ki67-positive cells. (**H**) Statistical analysis of the percentages of Ki67-positive cells (n = 3 independent samples, $^{**}P < 0.01$). (**I**) Immunostaining of Lgr5 for endogenous MSCs distribution 7 day after the implantation. Scale bars, 200 μm. The dotted white lines indicate the top layer of SPS or ECM-SPS. The 3D surface plot represents the distribution and fluorescence intensity of Lgr5-positive cells. (**J**) Statistical analysis of the percentages of Lgr5-positive cells (n = 3 independent samples, $^{**}P < 0.01$).

regeneration of ECs, whereas the SPS group only showed sporadic regeneration of ECs, failing to form a continuous epithelial layer. At 8 weeks postoperatively, the regenerated endometrium at the surgery site was covered by intact luminal epithelium in both groups (Fig. 6, B and C). The histological results were also confirmed by immunohistochemical staining with epithelial cell adhesion molecule (EpCAM) (Fig. 6C). At 4 weeks postoperatively, the endometrium was significantly thicker in the ECM-SPS group compared with the SPS group, and the endometrial thicknesses of the SPS and ECM-SPS were similar to that of the normal control at 8 and 12 weeks after the surgery (Fig. 6E). In addition, the production of uterine glands is essential for pregnancy. With the elapse of repair time, the percentage of glands has increased gradually and became significantly higher in the ECM-SPS at 8 and 12 weeks postoperatively (Fig. 6, D and F). The above results have suggested that the ECM-SPS has promoted endometrial regeneration.

Through previous in vitro studies, we have demonstrated that the ECM-SPS could regulate the behaviors of stem cells. Here, we found

that ECs-derive ECM could promote endometrial cell proliferation at the initial stage of repair (Fig. 6, G and H). In addition, a large number of Lgr5-positive MSCs were involved in the uterine repair (Fig. 6I). More Lgr5-positive MSCs were noted in the ECM-SPS group (Fig. 6J). Notably, the Lgr5-positive MSCs have clustered along the top layer of ECM-SPS (ECM_{EC}-SIS, indicated by the white dotted lines) but dispersed in the SPS group. It suggested that the ECs-derived ECM could recruit endogenous stem cells to promote epithelium regeneration at the initial stage.

As for endometrial remodeling, tissue cross sections were stained with Masson's trichrome to evaluate the endometrium fibrosis by the collagen content at 4, 8, and 12 weeks postoperatively (Fig. 7, A and B). At 4 weeks after the surgery, the degree of fibrosis was higher in both the SPS and ECM-SPS groups. However, with the elapse of time, the deposited collagen content has gradually decreased. At 8 and 12 weeks after the surgery, collagen deposition in the ECM-SPS group became significantly lower compared with the SPS group. The above results are consistent with previous proteomic results in which ECM-SIS may inhibit fibrosis.

The smooth muscle regeneration was detected by immunofluorescence staining of α-SMA and myosin (Fig. 7, C to F). At 4 weeks postoperatively, a small amount of smooth muscle regeneration was noted at the intersection of the regenerated area in the SPS and ECM-SPS groups. The α-SMA– and myosin-positive area of the ECM-SPS group was significantly larger compared with the SPS group. At 8 weeks postoperatively, a thin smooth muscle bundle has appeared in both groups, and the α-SMA–positive area in the ECM-SPS group was significantly larger compared with the SPS group. At 12 weeks postoperatively, a thin smooth muscle layer has formed in both groups, although more myosin-positive smooth muscles were noted in the ECM-SPS group. The above results suggested that both SPS and ECM-SPS scaffolds could induce smooth muscle regeneration, although the SMC-derived

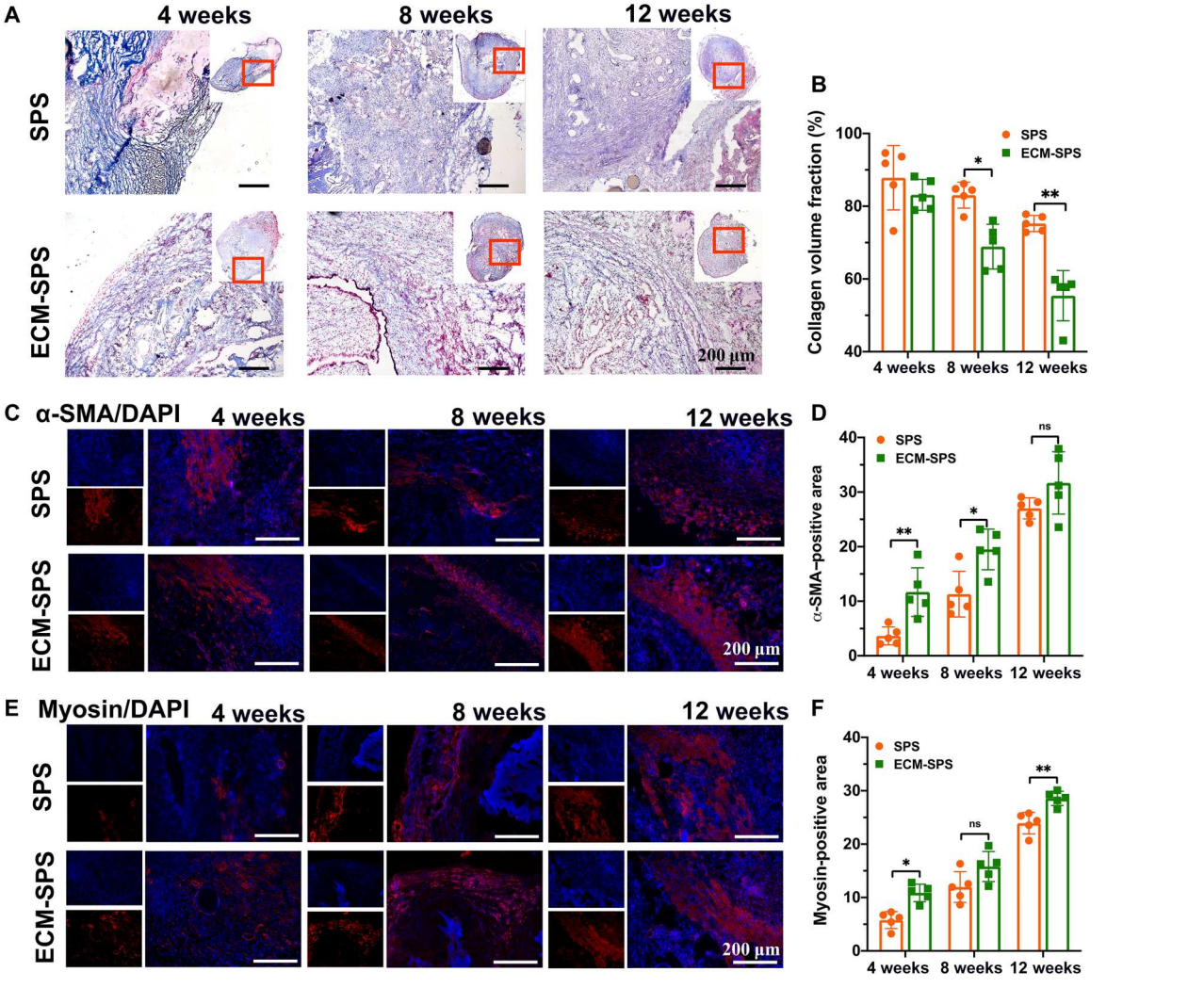

Fig. 7. The collagen remodeling and smooth muscle regeneration by various interventions. (**A**) Masson's trichrome staining of the reconstructed uterine segments. Scale bars, 200 μm. (**B**) Statistical analysis of collagen volume fraction on the Masson's trichrome–stained slides ($n = 5$ independent samples, $^*P < 0.05$ and $^{**}P < 0.01$). (**C**) Immunostaining of α-SMA for myometrium regeneration in the reconstructed uterine segments. Scale bars, 200 μm. (**D**) Statistical analysis of α-SMA–positive area ($n = 5$ independent samples, $^*P < 0.05$, $^{**}P < 0.01$, and ns). (**E**) Immunostaining of myosin for myometrium regeneration in the reconstructed uterine segments. Scale bars, 200 μm. (**F**) Statistical analysis of myosin positive area ($n = 5$ independent samples, $^*P < 0.05$, $^{**}P < 0.01$, and ns).

ECM could further promote the regeneration in the early stage of repair and maturation in the late stages of the repair in vivo.

Functional recovery of the reconstructed uterus

The ovary is an important component of the reproductive system. In this study, the effect of the SPS and ECM-SPS on the ovarian functions was evaluated by estrous cycles and follicle counts at all levels. From 12 weeks postoperatively, we have monitored vaginal smears for 14 days to test the estrous cycle of each group. As shown in Fig. 8A, a continuous and complete estrous cycle was established in both SPS and ECM-SPS groups, indicating that the secretary function of the ovaries was unaffected. Thereafter, the ovaries were sampled for histological staining, and the number of follicles was counted. As shown, there was no significant difference in the number of follicles after the repair between the experimental and control groups (Fig. 8B). These proved that both SPS and ECM-SPS were safe and did not affect the function of the ovaries.

To investigate the in vivo function of the repaired uterine tissue, we allowed female rats to mate with male rats 12 weeks after the uterine reconstruction. The reproductive outcomes are depicted in Fig. 8C and Table 1, which excludes cases where normal conception is not possible. As shown, the pregnant rate of the ECM-SPS group was higher than the SPS group but lower than the normal group. The average weight of embryos from the SPS and ECM-SPS groups was comparable to that of the normal controls, suggesting that the repaired uteri could sustain normal fetal development. Histological analyses had confirmed normal uterine tissue structure and placental development (Fig. 8D). These indicated that the

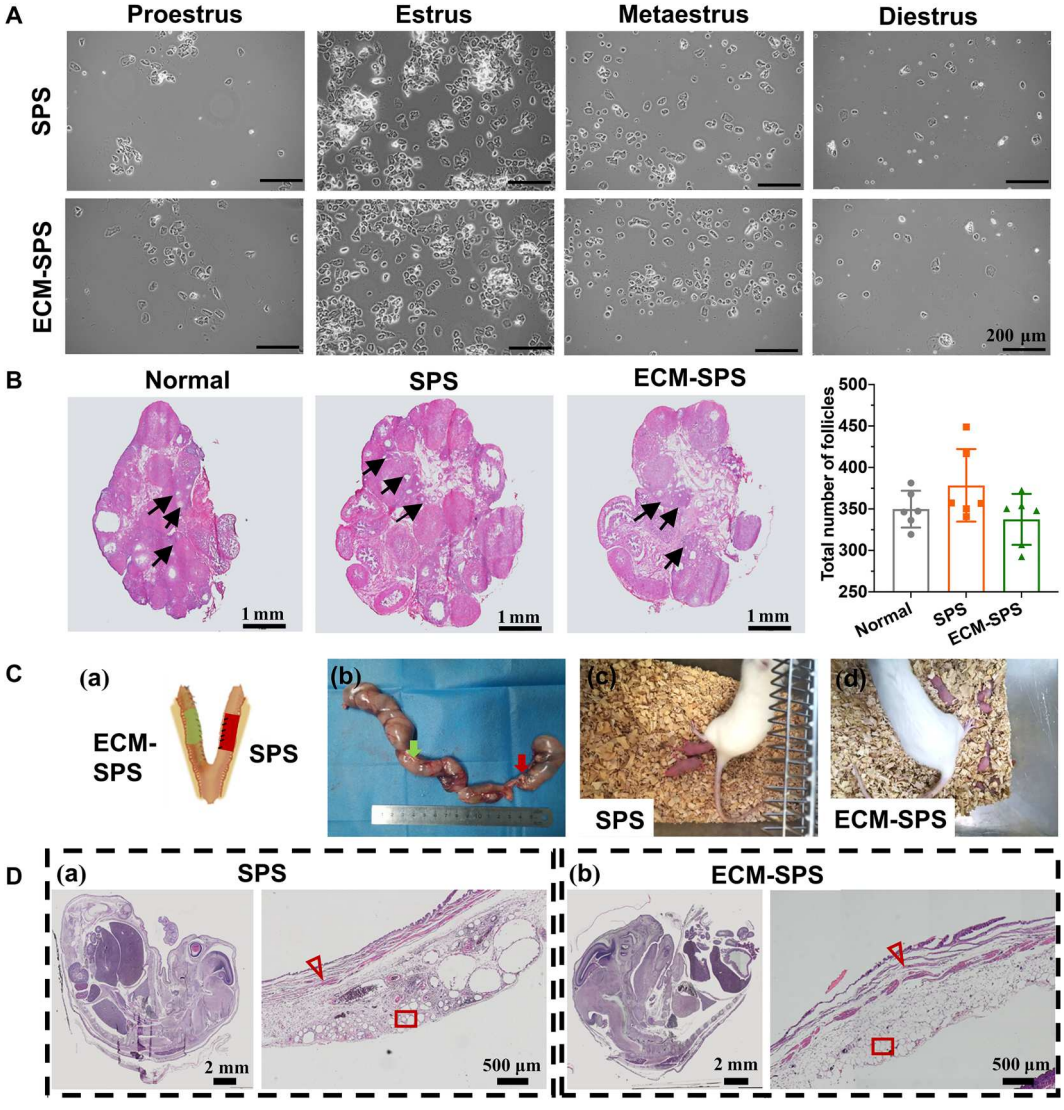

Fig. 8. Fertility restoration of the reconstructed uterine. (**A**) Vaginal smears which may reflect the changes in postoperative estrous cycles. Scale bars, 200 μm. (**B**) Histological analysis of the ovarian morphology and statistical analysis of the follicle numbers ($n = 6$ independent samples). Scale bars, 1 mm. (**C**) General view of the rat uterus containing embryos from the SPS (right, red arrow) and ECM-SPS (left, green arrow) groups (Ca). The arrows indicated scaffold (Cb). Images of the mother and newborn rats [(Cc) and (Cd)]. (**D**) H&E staining of the cross sections of the embryos (left; scale bars, 2 mm) and pregnant bioengineered uterus (right; scale bars, 500μm). The triangles represent myometrium, and rectangles represent decidualized endometrium.

Table 1. Number of fetuses, pregnancy rate, and fetal weight in surgically treated rats 19 days after mating with male rats.

	Normal control (n = 8)	ECM-SPS (n = 8)	SPS (n = 9)	P value
Pregnancy rate (%)	100%	75%	44.44%*	0.022†
Average litter per pregnancy (means ± SD)	10.13 ± 0.99	5.38 ± 4.44	2.00 ± 2.94*	0.0008‡
Fetal weight (g) (means ± SD)	4.50 ± 0.26	4.53 ± 1.84	4.96 ± 1.23	0.5854§

*P < 0.05. SPS group versus normal controls. †Fisher's exact test. ‡Kruskal-Wallis test. §One-tailed one-way ANOVA test. Data are presented as means ± SD.

ECM-SPS has attained a better effect for the repair of full-thickness uterine injury. The repaired uterus could sustain the tension during normal pregnancy and support embryonic development to the full term (Fig. 8C).

DISCUSSION

Developing a scaffold with structural properties and biological environment similar to those of natural tissue is crucial for the repair of full-thickness defect. In this study, we have constructed a ECM-SPS by simulating the structure and microenvironment of the uterine tissue. The ECM-SPS scaffold had the ECM microenvironment signatures of both the endometrium and myometrium and promoted the adhesion, proliferation, and lineage-directional differentiation of the MSCs, as well as the regeneration of endometrium and smooth muscle in subtotal uterine reconstruction.

In this study, the SIS and PU/SIS were selected as the biomimetic endometrium and biomimetic myometrium to construct the double-layer scaffold (SPS). As shown in Fig. 1, SPS has a dense intimal layer, which can be used as a physical barrier against adhesion, and has good supporting performance, which can maintain the structure of uterine cavity and avoid the occurrence of IUA (fig. S9). In addition, the PU/SIS emits autofluorescence at 405, 488, and 561 nm (fig. S10). To clearly display the position of the PU/SIS or ECM_{SMC}-PU/SIS in the regeneration area, a Cy5-labeled fluorescent secondary antibody was used to distinguish the cells from the scaffold. As shown in Fig. 6, the PU/SIS and ECM_{SMC}-PU/SIS have both been displayed with blue fluorescence. Most endometrial epithelium has regenerated along the SIS or ECM_{EC}-SIS (Fig. 6C), while more smooth muscle has regenerated around with the PU/SIS or ECM_{SMC}-PU/SIS (Fig. 7, C and E). This result confirmed the rationality of the design of double-layer scaffold and the selection of materials in this study.

The uterine tissue contains various types of cells including MSCs, fibroblasts, immune cells, vascular endothelial cells, etc. The selection of appropriate tissue cells is the key to the successful construction of an ECM biomimetic scaffold. Previous studies have mostly focused on the roles of MSC-derived ECM on the regeneration (*34*–*37*), and few have explored tissue-specific functional cell–derived ECM. In this study, tissue functional cells have been used for the construction of the ECM biomimetic microenvironment. Different from common cell components, tissue functional cells are important component of the tissue with a physiological role. The proteins they secrete are specific to the tissue and more similar to the ECM microenvironment of the natural tissue (*34*, *38*–*40*). These cells also constitute an important component of the stem cell niche that can regulate the fate of stem cells (*41*, *42*). Endometrial ECs are the main functional cells of the endometrium that is involved with embryonic implantation (*43*–*45*). Therefore, we have chosen the endometrial ECs and SMCs as the functional cells to modify the bilayer SPS scaffold and proved that the tissue functional cell–derived ECM has successfully constructed the tissue-specific microenvironment and had similar properties of the MSC lineage–directional induction with tissue-derived ECM (Fig. 4, D to G).

The uterus has cyclic regenerative properties. In response to regulatory hormones, its tissue continues to undergo dynamic remodeling, along with significant changes in the phenotype of endometrial cells. In the proliferative phase, these cells are in a state of rapid proliferation, and the expression of proteins associated with uterus regeneration, such as Ki67, CDC20B, CCNO, Wnt etc., is significantly higher than that in the secretary phase (*46*). During the secretary phase, endometrial cells are affected by progesterone, resulting in great changes in cell phenotypes including tight junctions, polarity, etc., which are more conducive to embryonic implantation (*46*). Therefore, in this study, the ECs from the proliferative stage were selected to construct the scaffold for endometrial regeneration. Analysis of our proteomic results showed that ECM_{EC}-SIS carries significant characteristics of the endometrial ECM microenvironment in the proliferative phase. It contained abundance of *Wnt* signaling pathway proteins such as Wnt2, Wnt5a/5b, etc. (fig. S5), which are highly expressed in the proliferative stage (*46*). On the other hand, dickkopf-related protein 1 (DKK1), a typical *Wnt* pathway inhibitor expressed in the secretary phase (*46*), was not detected in the ECM_{EC}-SIS (fig. S5).

The ECM modified on the scaffold surface significantly changed the ECM microenvironment, surface morphology, and physical properties of the scaffold surface. It can be seen that the hydrophilicity of the PU/SIS after the ECM modification was significantly enhanced (Fig. 2F), resulting in a significant increase in cell adhesion and better tissue integration (Figs. 4A and 5A). In addition, the ECM modification has a great impact on the elastic modulus of the scaffold. The elastic modulus of the ECM_{EC}-SIS was lower than that of the SIS, while the ECM_{SMC}-PU/SIS was higher than that of the PU/SIS (Fig. 2G and fig. S4B). Studies have shown that the MSCs tend to differentiate into epithelium and maintain the characteristics of epithelium on the soft matrix (*47*, *48*), while increased hardness of the matrix is more conducive to myogenic differentiation (*49*), which was in keeping with our results (Fig. 4, D to G). This suggested that the changes of the scaffold mechanical properties induced by the ECM modification may be an important factor for the induction of tissue-specific regeneration.

The composition of matrisome proteins is quite different for each ECM tissue type, and the unique sets of dECM proteins

represent vital tissue–specific proteins that are crucial for cell growth and differentiation during tissue and organ remodeling (*19*, *50*, *51*). The ECM produced by the ECs and SMCs also has a relatively complex composition and displays unique matrisome signature (Fig. 3). The unique sets of dECM proteins in the ECM_{EC}-SIS and ECM_{SMC}-PU/SIS may be critical for cell growth and differentiation. In this study, both the ECM_{EC}-SIS and ECM_{SMC}-PU/SIS showed great potential for cell adhesion and proliferation, in addition with substantial difference in their tissue-inducing properties (Fig. 4). To explore the possible reasons for the difference in the tissue-inducing properties of the ECM_{EC}-SIS and ECM_{SMC}-PU/SIS, we have used the MatrisomeDB database to classify and briefly analyze the identified proteins. Collagen types were similar in the ECM_{SMC}-PU/SIS and ECM_{EC}-SIS, and the largest difference was found with COL3 (fig. S5). As a fibrillar collagen, the COL3 is highly expressed in the endometrium and involved in blood vessel development, embryonic development, and neuron migration (*52*) and holds a great significance for endometrial regeneration. A recent study showed that COL3 can binds with TGF-β in a dose-dependent manner to attenuate TGF-β signaling, showing a significant inhibitory effect on tissue fibrosis (*31*). In this study, the high expression of COL3 in the ECM_{EC}-SIS may account for the lower level of fibrosis in the ECM-SPS during the repair of uterine injury. In addition, among the factors secreted in the ECM_{EC}-SIS, members of Wnt family, Wnt2 and Wnt5a/5b, were significantly higher compared with the ECM_{SMC}-PU/SIS (fig. S5). The Wnt pathway is critical for uterine development and can modulate the process of regeneration during the estrous cycle (*53*, *54*). The highly expressed Wnt family members in the ECM_{EC}-SIS may therefore play a constructive role in epithelium regeneration. Furthermore, gene set enrichment analysis showed that the MET signal pathway was significantly up-regulated in the ECM_{EC}-SIS, which could promote the transformation of mesenchymal to epithelium (Fig. 3H).

As the main component of ECM of the smooth muscle tissue, COL1 has shown a great potential for inducing the differentiation of placenta-derived multipotent cells into the SMCs (*54*). In this study, our proteomic analysis also showed COL1A1 to be the most abundant collagen in the ECM_{SMC}-PU/SIS (fig. S5). In the ECM glycoprotein subset, the expression of FN was most abundant in the ECM_{SMC}-PU/SIS, which was also significantly higher than that in the ECM_{EC}-SIS (fig. S5). As a multifunctional adhesive glycoprotein, FN plays an important role in tissue repair by regulating cell attachment and motility, as well as embryogenesis (*55*). A study by Jain *et al.* (*56*) has found that FN can promote neointima formation in vivo by potentiating SMCs proliferation and migration through activation of focal adhesion kinase/Src and Akt1/mammalian target of rapamycin signaling. In another study by Klingberg *et al.* (*57*), FN has immobilized latent LTBP1 and thereby stored TGF-β in the ECM, which might have played an important role in the induction of placenta-derived multipotent cell differentiation into the SMCs by enhancing the TGF-β signal pathway. Furthermore, gene set enrichment analysis exhibited that the TGF-β signal pathway, which is pivotal for smooth muscle differentiation, was also up-regulated in the ECM_{SMC}-PU/SIS (Fig. 3I).

The role of the ECM is complex, and the above speculation based on literature survey and analyses does not prove how the tissue-specific microenvironment we constructed has worked, nor is it clear that ECM protein has played a major role. For the next step, we will conduct an in-depth analysis of the proteomic results to explore the key ECM proteins that have endowed the tissue-inducing properties.

In this study, a bilayer ECM-SPS scaffold has been constructed by combining a bionic uterine structure with an ECM microenvironment to fulfill the multiple requirements for uterus repairing. The design of multilayered bionic scaffold has provided a better option for simultaneous regeneration of both the endometrium and myometrium. The cell-derived ECM can mimic the tissue-specific ECM microenvironment, recruit induced endogenous stem cells, and promote orderly tissue regeneration. Our approach has therefore opened a new revenue for the prevention and treatment of severe IUA and may provide a new strategy for the development of inducible biomaterials for the repair and reconstruction of the bladder, urethra, esophagus, airway and other multilayered tissues.

MATERIALS AND METHODS

Study design

Severe IUAs are often accompanied by the damage of myometrium and may result in thinning of the uterus, reduction of mechanical strength, and formation of adhesion between the wounds. It is important to provide appropriate mechanical support, create an antiadhesion barrier, and promote simultaneous regeneration of the endometrium and smooth muscle to prevent severe IUA. Inspired by the nature of uterus, we developed a bilayer scaffold (ECM-SPS) with biomimetic heterogeneous features and ECM microenvironment for IUA with myometrial damage, so as to fit the multiple needs in uterus repairing. The SIS with a seamless structure was selected as the bionic endometrium to provide an antiadhesive barrier and a substrate for the adhesion and proliferation of ECs. The PU/SIS composites with similar elastic modulus to the uterus were selected as the bionic myometrium to provide appropriate mechanical support. Further, tissue-specific cell–derived ECM was modified on the SPS to biomimetic ECM environment for functional regeneration of the uterus.

Preparation and characterization of the SPS and ECM-SPS

The SIS and PU/SIS were prepared with our previously described methods (*12*, *13*), which is described in detail in the Supplementary Materials. The prepared SIS and the PU/SIS were respectively cut into squares with a size of 20 × 20 mm and quadrangles with a length of 20 mm and a thickness of 300 μm. The PU emulsion was used to stick the SIS onto the PU/SIS to prepare a SPS scaffold.

Uterine ECs, SMCs, and MSCs were purchased from iCell Bioscience Inc., Shanghai, China. To prepare the ECM-modified scaffold, the prepared cells were first cocultured with the scaffolds for the secretion of ECM. The scaffolds were then decellularized. Thereafter, the SIS and PU/SIS were immersed with phosphate-buffered saline (PBS) for 12 hours. A total of 1×10^5 ECs were seeded onto the SIS and cultured with epithelial culture medium (EpiCM) for 7 days for the secretion of EC-specific ECM. A total of 4×10^5 of SMCs were seeded onto the PU/SIS and cultured with smooth muscle culture medium (SMCM) for 14 days for the secretion of SMC-specific ECM. The above cells were evenly cultured on both sides of the SIS or PU/SIS. Thereafter, the cell-scaffold composites were frozen at −80°C for 40 min and thawed at 37°C for 40 min, following by washing three times in PBS. The freeze/thaw (−80°C/37°C) cycle was repeated twice. Thereafter, the composites

were treated with preheated 1% Triton X-100 at 37°C for 5 min and washed three times with PBS. Thereafter, the derived ECM_{EC}-SIS and $ECM_{PU/SIS}$-PU/SIS were freeze-dried. The whole decellularized process was performed gently and with care. The PU emulsion was used to stick the ECM_{EC}-SIS onto the $ECM_{PU/SIS}$-PU/SIS to derive an ECM-SPS scaffold.

Each batch of samples is analyzed by scanning electron microscope (SEM) and total protein content. Samples meeting the following criteria will be used for subsequent research: (i) SEM shows obvious ECM attachment; (ii) the total protein content of ECM_{EC}-SIS exceeds 1000 μg/cm^2; and (iii) the total protein content of ECM_{SMC}-PU/SIS exceeds 500 μg/cm^2.

In vitro adhesion tests

For the peeling adhesion test, the adhered samples with a width of 10 mm were prepared and tested by the standard 180° peel test (Fig. 1B). All tests were conducted with a constant peeling speed of 10 mm/min. The measured force has reached a plateau as the peeling process entered the steady state. The adhesive sheer strength was calculated with the following Eq. 1

$$\text{Peel strength} = \frac{\text{Plateau Force}}{\text{Width}} \quad (1)$$

Scanning electron microscope

An SEM was used to observe the morphology of the SPS and ECM-SPS. The samples were freeze-dried for 24 hours and brittle-fractured with liquid nitrogen to obtain its cross section. After sprayed with gold, the samples were observed by SEM (EVO 10, ZEISS) at an accelerating voltage of 15 kV.

Atomic force microscopy

An atomic force microscopy (AFM) was used to observe the morphology and elastic modulus of the SPS and ECM-SPS. The surface topology and elastic modulus maps of the scaffold were recorded on SPM-9700HT and analyzed using the Nano 3D Mapping software. All morphology images were recorded using a tapping mode in the ambient atmosphere. The approximate resonance frequency of the cantilever was 280 kHz, and the force constant was around 60 N/m. The elastic modulus of scaffold was estimated with a 2.5-μm radius, sphere-tipped AFM tip. The spring constant of the AFM tip was determined at ~120 pN/nm. The samples were indented at low indentation rate (0.5 Hz) with a trigger force of 5 nN.

Evaluation of the decellularization efficiency

To assess the effect of decellularization, the DNA content, total ECM protein, collagen, and GAG were quantified. Each sample was measured three times, and the average absorbance value was calculated.

The residual DNA content was determined by DAPI (1 μg/ml; P36931, Invitrogen) staining and quantified by a DNA assay. Briefly, the samples were fixed with 4% formaldehyde for 10 min at room temperature and washed three times in PBS. Thereafter, they were immersed in a DAPI solution (1 μg/ml; P36931, Invitrogen) for 5 min at 37°C. After the washing, the samples were imaged under a confocal microscope (Nikon A1RMP+, Nikon Instruments Inc.). The DNA content was quantified by using a Quan PicoGreen dsDNA Assay Kit (P7581, Invitrogen) by following the instructions of the manufacturer.

The samples were then crushed in liquid nitrogen with a freezer mill (6700, SPEX SamplePrep). Approximately 10 mg of sample powder was lysed in 150 μl of intensive radioimmunoprecipitation assay buffer (P003B, Beyotime Biotechnology) overnight at 4°C, and centrifuged at 12,000 rpm for 10 min. The supernatant was collected for the determination of protein content with a bicinchoninic acid (BCA) protein assay kit (P0012, Beyotime Biotechnology) by following the instructions from the manufacturer. The precipitation was resuspended in a solution (100 μl) containing 8 M urea, 100 mM ammonium bicarbonate, and 10 mM dithiothreitol at pH 8.0 under agitation at 37°C for 2 hours. The supernatant was collected for the determination of protein content using a BCA protein assay kit. The collagen content was quantified with a hydroxyproline assay kit (K555-100, BioVision) with a protocol provided by the manufacturer. The concentration of each sample was determined against a hydroxyproline standard. Sulfated GAG concentration was measured by using a dimethylmethylene blue assay kit (JM9048, Hepeng Biological) with a protocol provided by the manufacturer.

The samples powder was incubated in 0.5% bovine serum albumin/PBS solution for 24 hours at 37°C and centrifuged at 12,000 rpm for 10 min. The supernatant was collected for determining the concentrations of EGF, TGF-β, PDGF-BB, and HGF with EGF enzyme-linked immunosorbent assay (ELISA) kit (ELH-VEGF-1, RayBiotech), TGF-β ELISA kit (ELH-TGFb1-1, RayBiotech), PDGF-BB ELISA kit (ELH-PDGFBB-1, RayBiotech), and HGF ELISA kit (ELH-HGF-1, RayBiotech), respectively.

Hydrophilicity assay

The hydrophilicity was indicated by water contact angle. Approximately 10 μl of deionized water was dropped onto the surface of the materials, and the static water contact angle was measured with a contact angle goniometer (OCA 15/20, Future Digital Scientific Corp.).

Proteomic analysis

The technical support of proteomic analysis was provided by Shanghai Applied Protein Technology Co. Ltd. dECM components identified by the mass spectrometry were also annotated with human matrix MatrisomeDB (https://matrisomedb.org) to identify matrix body proteins in each decellularized tissue type (*44*, *58*). Functional enrichment analysis was carried out using Metascape (http://metascape.org) (*59*). Gene set enrichment analysis was performed with Gene Set Enrichment Analysis software version 4.3.2 (*60*).

Cell adhesion, viability, and proliferation on scaffolds in vitro

The MSCs were seeded onto the surface of the materials at a density of 5×10^4 cells/cm^2. After 6 hours of incubation, the cell-scaffold samples were washed with PBS and stained with Cy5-phalloidine (40762ES75, Yeasen Biotechnology) and DAPI for 10 min at 37°C. After the washing, the samples were imaged under a confocal microscope (Nikon A1RMP+, Nikon), determining the location of the cell by the cytoskeleton. Three samples were selected for each group, and three random fields per sample were investigated by photomicrography at a magnification of ×40.

The viability and proliferation of the MSCs on the SPS and ECM-SPS were determined by live/dead staining and CCK8 assay,

respectively. Briefly, the MSCs were seeded onto the surface of the materials at a density of 1×10^5 cells/cm^2 for 3 days. The cell-scaffold composites were washed three times with PBS and stained with Calcein-AM and propidium iodide double stain kit (L3224, Invitrogen) for 20 min at 37°C in the darkness. The samples were then imaged under a confocal microscope (Nikon A1RMP+, Nikon). The extract solution was prepared by soaking the samples in a complete medium (surface area:volume, 1:6) at 37°C for 24 hours. Meanwhile, the MSCs were seeded onto a 96-well plate at a density of 5×10^3 cells per well and cultured with Dulbecco's modified Eagle's medium (DMEM) medium containing 15% fetal bovine serum. Thereafter, extract solution was replaced by cultured cells for 7 days. The proliferation of the MSCs was tested on days 1, 3, 5, and 7 with a CCK8 kit (CK04, Dojindo) by following the manufacturer's protocol.

Cytoskeleton organization was visualized by fluorescence staining with rhodamine-phalloidin. The MSCs were seeded onto the surface of the materials at a density of 5×10^4 cells/cm^2. After 3 days of incubation, the cell-scaffold samples were fixed with 4% formaldehyde for 10 min at room temperature and washed three times in PBS. Thereafter, the samples were treated with 0.1% Triton X-100 and incubated with rhodamine-phalloidin (40762ES75, Yeasen Biotechnology) and DAPI. After the washing, the cell morphology was visualized under a confocal laser microscope (Nikon A1RMP+, Nikon Instruments Inc.).

Differentiation of the MSCs induced by the scaffolds

A total of 1×10^5 MSCs were seeded onto the ECM_{EC}-SIS and cultured with EpiCM medium, with the MSCs cultured with the SIS as the negative control. A total of 4×10^5 SMCs were seeded onto the ECM_{SMC}-PU/SIS and cultured with SMCM medium, with the MSCs cultured with the PU/SIS as the negative control.

After 7 days of culture, the cell-scaffold composites were fixed in 4% (v/v) paraformaldehyde solution for 10 min, treated with 0.1% Triton X-100 for 15 min, and incubated with 5% goat serum for 30 min at 37°C. They were then incubated with a specific anti–E-Cadherin (1:200; ab40772, Abcam), anti-CK18 (1:200; ab133263, Abcam), anti–α-SMA (1:200; ab7817, Abcam), and anti-myosin (1:100; ab182981, Abcam) overnight at 4°C. Subsequently, the samples were treated with goat anti-mouse secondary antibody (1:500; 115-605-003, Jackson ImmunoResearch) or goat anti-rabbit secondary antibody (1:500; 111-605-003, Jackson ImmunoResearch) at 37°C for 1 hour. The nuclei were counterstained with DAPI (1 μg/ml; P36931, Invitrogen) for 5 min at room temperature. Thereafter, the samples were imaged under a confocal microscope (Nikon A1RMP+, Nikon Instruments Inc.,).

After 3 and 7 days of culture, the MSCs were isolated from cell scaffolds and lysed in TRIzol reagent by following the manufacturer's protocol, followed by reverse transcription (RR047, Takara). Quantitative polymerase chain reaction was carried out using SYBR Green master mix (RR820, Takara) on a real-time thermocycler (LC 96, Roche). All samples were analyzed in triplicate. Expression of the target genes was normalized with that of *GAPDH* gene. The polymerase chain reaction primers were listed in table S1. The relative expression folds were calculated with a $2^{-\Delta\Delta Ct}$ method.

Characterization of cell infiltration, vascularization, and immune response in vivo

The histocompatibility of the SPS and ECM-SPS in vivo was investigated through subcutaneous implantation experiments. Two separate skin incisions were made on the back of SD rats ($n = 6$). Thereafter, the SPS and ECM-SPS were carefully implanted into the subcutaneous pockets. The animals were euthanized 4 weeks after the surgery. The implants and surrounding tissues were collected and fixed with 4% paraformaldehyde solution for histological evaluation. Sections was prepared and subjected to H&E and DAPI staining to evaluate the cell infiltration. To assess vascularization, serial sections were immunolabeled with CD31 (1:50; ab182981, Abcam). To identify the phenotype of the macrophages, immunofluorescence staining was carried out with CD86 (1:200; ab119857, Abcam) and CD206 (1:500; ab64693, Abcam), which are markers for M1-like and M2-like macrophages. Subsequently, the samples were treated with goat anti-mouse secondary antibody (1:200, 115-605-003, Jackson ImmunoResearch) or goat anti-rabbit secondary antibody (1:200, 111-605-003, Jackson ImmunoResearch) at 37°C for 1 hour. The nuclei were counterstained with DAPI for 5 min at room temperature.

Reconstruction of subtotal uterine

All animal experiments have been conducted to conform to the guidelines of the Experimental Animals Management Committee of Sichuan Province and approved by Sichuan University Animal Care and Use Committee (no. 2019023A).

Mature female Sprague-Dawley (SD) rats weighing 250 to 300 g each with consecutive estrus cycles were included in the experiment and those in diestrus were used for the experiment. Ninety-six uterine horns were randomly assigned into excision group, SPS group, and ECM-SPS group. All rats were anesthetized with pentobarbital sodium, and a low abdominal midline incision was made to expose the uterine horns. As shown in Fig. 6A, a segment of 1.5 cm in length and 1/2 of the total circumference was resected from the horn of the uterus, with the side of mesometrium left intact. The scaffolds (1.5 cm × 0.5 cm) were sutured to replace the excised segment. The rats from the excision group were subjected to no treatment. After surgery, all rats had received intramuscular injections of penicillin twice a day for 3 days.

Histological analysis

At 4, 8, and 12 weeks after the surgery, the animals were euthanized. The operative area of each uterine horn was prepared and subjected to H&E and Masson's trichrome staining. The thickness of the uterine endometrium was measured using ImageJ software.

For immunofluorescence staining, serial sections were immunolabeled with anti–EpCAM (1:200; ab221552, Abcam), Lgr5 (1:200; ab219107, Abcam), Ki67 (1:200; ab15580, Abcam), anti-α-SMA (1:200; ab7817, Abcam), anti-myosin (1:100; ab182981, Abcam), and FoxA2 (1:200; ab108422, Abcam). ImageJ software was used for analyzing the images, including the percentage of positive stained areas and glands. The percentage of glands was calculated with the following Eq. 2

$$\text{The percentage of glands}(\%) = \frac{\text{Gland number in regenerative region}}{\text{Gland number in undamaged region of the same cornu uteri}} \times 100\% \quad (2)$$

Functional studies

The function of the reconstructed uterus was assessed by determining its receptiveness to the blastocysts implantation, support for the embryos to the late stages of pregnancy, and its effect on the ovarian function, including the morphology and estrous cycles. After 12 weeks postoperatively, the rats were allowed to mate, and fertilization was confirmed by the presence of a vaginal plug ($n = 10$ uterine horns per group). The animals were euthanized at mid-to-late gestation and examined for the numbers of uterine horns and position of the embryos. Rats with normal fertility were included in statistical analysis. For ovarian function studies, vaginal smears were collected daily from 8:00 to 10:00 a.m. to analyze the changes in the rat estrous cycle. The morphology of the ovaries was observed by H&E staining, and the number of follicles at each level was counted.

Statistical analysis

All results were presented as means ± SD. Single comparison was carried out with an independent sample *t* test. Comparison of three or more groups was carried out using one-way analysis of variance (ANOVA). Nonparametric analogs were applied for ordinal categorical variables. Fisher's exact test was performed to compare pregnancy rates. *n* was considered the number of times an experiment was independently performed. ns represents no significance. $P < 0.05$ was considered to be statistically significant.

Supplementary Materials

This PDF file includes:

Supplementary Methods
Figs. S1 to S10
Table S1
Data S1 and S2

REFERENCES AND NOTES

1. AAGL Elevating Gynecologic Surgery, AAGL practice report: Practice guidelines on intrauterine adhesions developed in collaboration with the European Society of Gynaecological Endoscopy (ESGE). *Gynecol. Surg.* **14**, 6 (2017).
2. C. A. Salazar, K. Isaacson, S. Morris, A comprehensive review of Asherman's syndrome: Causes, symptoms and treatment options. *Curr. Opin. Obstet. Gynecol.* **29**, 249–256 (2017).
3. X. Zhang, W. Liu, Y. Zhou, J. Qiu, Y. Sun, M. Li, Y. Ding, Q. Xi, Comparison of therapeutic efficacy of three methods to prevent re-adhesion after hysteroscopic intrauterine adhesion separation: A parallel, randomized and single-center trial. *Ann. Palliat. Med.* **10**, 6804–6823 (2021).
4. L. Wang, C. Yu, T. Chang, M. Zhang, S. Song, C. Xiong, P. Su, W. Xiang, In situ repair abilities of human umbilical cord-derived mesenchymal stem cells and autocrosslinked hyaluronic acid gel complex in rhesus monkeys with intrauterine adhesion. *Sci. Adv.* **6**, eaba6357 (2020).
5. Z. Yin, J. Wang, W. Cui, C. Tong, Advanced biomaterials for promoting endometrial regeneration. *Adv. Healthc. Mater.* **12**, e2202490 (2023).
6. A. B. Hooker, M. Lemmers, A. L. Thurkow, M. W. Heymans, B. C. Opmeer, H. A. M. Brolmann, B. W. Mol, J. A. F. Huirne, Systematic review and meta-analysis of intrauterine adhesions after miscarriage: Prevalence, risk factors and long-term reproductive outcome. *Hum. Reprod. Update* **20**, 262–278 (2014).
7. M. Cheng, W. H. Chang, S. T. Yang, H. Y. Huang, K. H. Tsui, C. P. Chang, W. L. Lee, P. H. Wang, Efficacy of applying hyaluronic acid gels in the primary prevention of intrauterine adhesion after hysteroscopic myomectomy: A meta-analysis of randomized controlled trials. *Life (Basel)* **10**, 285 (2020).
8. X. R. Zhang, Y. Z. Huang, H. W. Gao, Y. L. Jiang, J. G. Hu, J. K. Pi, A. J. Chen, Y. Zhang, L. Zhou, H. Q. Xie, Hypoxic preconditioning of human urine-derived stem cell-laden small intestinal submucosa enhances wound healing potential. *Stem Cell Res. Ther.* **11**, 150 (2020).
9. X. Z. Zhang, Y. L. Jiang, J. G. Hu, L. M. Zhao, Q. Z. Chen, Y. Liang, Y. Zhang, X. X. Lei, R. Wang, Y. Lei, Q. Y. Zhang, J. Li-Ling, H. Q. Xie, Procyanidins-crosslinked small intestine submucosa: A bladder patch promotes smooth muscle regeneration and bladder function restoration in a rabbit model. *Bioact. Mater.* **6**, 1827–1838 (2021).
10. M. Wang, Y. Q. Li, J. Cao, M. Gong, Y. Zhang, X. Chen, M. X. Tian, H. Q. Xie, Accelerating effects of genipin-crosslinked small intestinal submucosa for defected gastric mucosa repair. *J. Mater. Chem. B* **5**, 7059–7071 (2017).
11. J. C. Luo, W. Chen, X. H. Chen, T. W. Qin, Y. C. Huang, H. Q. Xie, X. Q. Li, Z. Y. Qian, Z. M. Yang, A multi-step method for preparation of porcine small intestinal submucosa (SIS). *Biomaterials* **32**, 706–713 (2011).
12. L. Da, M. Gong, A. Chen, Y. Zhang, Y. Huang, Z. Guo, S. Li, J. Li-Ling, L. Zhang, H. Xie, Composite elastomeric polyurethane scaffolds incorporating small intestinal submucosa for soft tissue engineering. *Acta Biomater.* **59**, 45–57 (2017).
13. L. M. Zhao, L. Wang, W. Q. Zhang, R. Wang, X. Z. Zhang, X. X. Lei, Y. Liang, Y. T. Song, Q. Y. Zhang, K. Lin, H. Q. Xie, Promotion of right ventricular outflow tract reconstruction using a novel cardiac patch incorporated with hypoxia-pretreated urine-derived stem cells. *Bioact. Mater.* **14**, 206–218 (2022).
14. S. Xu, R. W. S. Chan, T. Li, E. H. Y. Ng, W. S. B. Yeung, Understanding the regulatory mechanisms of endometrial cells on activities of endometrial mesenchymal stem-like cells during menstruation. *Stem Cell Res. Ther.* **11**, 239 (2020).
15. J. Cen, Y. Zhang, Y. Bai, S. Ma, C. Zhang, L. Jin, S. Duan, Y. Du, Y. Guo, Research progress of stem cell therapy for endometrial injury. *Mater. Today Bio.* **16**, 100389 (2022).
16. M. A. Ruehle, E. A. Eastburn, S. A. LaBelle, L. Krishnan, J. A. Weiss, J. D. Boerckel, L. B. Wood, R. E. Guldberg, N. J. Willett, Extracellular matrix compression temporally regulates microvascular angiogenesis. *Sci. Adv.* **6**, eabb6351 (2020).
17. Y. Peng, X. Qing, H. Lin, D. Huang, J. Li, S. Tian, S. Liu, X. Lv, K. Ma, R. Li, Z. Rao, Y. Bai, S. Chen, M. Lei, D. Quan, Z. Shao, Decellularized disc hydrogels for hBMSCs tissue-specific differentiation and tissue regeneration. *Bioact. Mater.* **6**, 3541–3556 (2021).
18. M. Chen, Y. Y. Li, S. Liu, Z. Feng, H. Wang, D. Yang, W. Guo, Z. Yuan, S. Gao, Y. Zhang, K. Zha, B. Huang, F. Wei, X. Sang, Q. Tian, X. Yang, X. Sui, Y. Zhou, Y. Zheng, Q. Guo, Hierarchical macro-microporous WPU-ECM scaffolds combined with microfracture promote in situ articular cartilage regeneration in rabbits. *Bioact. Mater.* **6**, 1932–1944 (2021).
19. B. Yao, R. Wang, Y. Wang, Y. Zhang, T. Hu, W. Song, Z. Li, S. Huang, X. Fu, Biochemical and structural cues of 3D-printed matrix synergistically direct MSC differentiation for functional sweat gland regeneration. *Sci. Adv.* **6**, eaaz1094 (2020).
20. M. L. Wong, J. L. Wong, N. Vapniarsky, L. G. Griffiths, In vivo xenogeneic scaffold fate is determined by residual antigenicity and extracellular matrix preservation. *Biomaterials* **92**, 1–12 (2016).
21. L. Hou, J. Coller, V. Natu, T. J. Hastie, N. F. Huang, Combinatorial extracellular matrix microenvironments promote survival and phenotype of human induced pluripotent stem cell-derived endothelial cells in hypoxia. *Acta Biomater.* **44**, 188–199 (2016).
22. A. Shakouri-Motlagh, A. J. O'Connor, S. P. Brennecke, B. Kalionis, D. E. Heath, Native and solubilized decellularized extracellular matrix: A critical assessment of their potential for improving the expansion of mesenchymal stem cells. *Acta Biomater.* **55**, 1–12 (2017).
23. X. D. Chen, V. Dusevich, J. Q. Feng, S. C. Manolagas, R. L. Jilka, Extracellular matrix made by bone marrow cells facilitates expansion of marrow-derived mesenchymal progenitor cells and prevents their differentiation into osteoblasts. *J. Bone Miner. Res.* **22**, 1943–1956 (2007).
24. M. Pei, F. He, V. L. Kish, Expansion on extracellular matrix deposited by human bone marrow stromal cells facilitates stem cell proliferation and tissue-specific lineage potential. *Tissue Eng. Part A* **17**, 3067–3076 (2011).
25. Y. Sun, W. Li, Z. Lu, R. Chen, J. Ling, Q. Ran, R. L. Jilka, X. D. Chen, Rescuing replication and osteogenesis of aged mesenchymal stem cells by exposure to a young extracellular matrix. *FASEB J.* **25**, 1474–1485 (2011).
26. K. H. Schneider, M. Enayati, C. Grasl, I. Walter, L. Budinsky, G. Zebic, C. Kaun, A. Wagner, K. Kratochwill, H. Redl, A. H. Teuschl, B. K. Podesser, H. Bergmeister, Acellular vascular matrix grafts from human placenta chorion: Impact of ECM preservation on graft characteristics, protein composition and in vivo performance. *Biomaterials* **177**, 14–26 (2018).
27. L. Fagerberg, B. M. Hallström, P. Oksvold, C. Kampf, D. Djureinovic, J. Odeberg, M. Habuka, S. Tahmasebpoor, A. Danielsson, K. Edlund, A. Asplund, E. Sjöstedt, E. Lundberg, C. A. K. Szigyarto, M. Skogs, J. O. Takanen, H. Berling, H. Tegel, J. Mulder, P. Nilsson, J. M. Schwenk, C. Lindskog, F. Danielsson, A. Mardinoglu, Å. Sivertsson, K. von Feilitzen, M. Forsberg, M. Zwahlen, I. M. Olsson, S. Navani, M. Huss, J. Nielsen, F. Ponten, M. Uhlén, Analysis of the human tissue-specific expression by genome-wide integration of transcriptomics and antibody-based proteomics. *Mol. Cell. Proteomics* **13**, 397–406 (2014).
28. L. Y. Sakai, D. R. Keene, R. W. Glanville, H. P. Bächinger, Purification and partial characterization of fibrillin, a cysteine-rich structural component of connective tissue microfibrils. *J. Biol. Chem.* **266**, 14763–14770 (1991).
29. S. Chakravarti, T. Magnuson, J. H. Lass, K. J. Jepsen, C. LaMantia, H. Carroll, Lumican regulates collagen fibril assembly: Skin fragility and corneal opacity in the absence of lumican. *J. Cell Biol.* **141**, 1277–1286 (1998).

30. S. Saika, A. Shiraishi, S. Saika, C. Y. Liu, J. L. Funderburgh, C. W. C. Kao, R. L. Converse, W. W. Y. Kao, Role of lumican in the corneal epithelium during wound healing. *J. Biol. Chem.* **275**, 2607–2612 (2000).
31. B. K. Brisson, D. C. Stewart, C. Burgwin, D. Chenoweth, R. G. Wells, S. L. Adams, S. W. Volk, Cysteine-rich domain of type III collagen N-propeptide inhibits fibroblast activation by attenuating TGFβ signaling. *Matrix Biol.* **109**, 19–33 (2022).
32. C. E. Gargett, K. E. Schwab, J. A. Deane, Endometrial stem/progenitor cells: The first 10 years. *Hum. Reprod. Update* **22**, 137–163 (2016).
33. W. Wang, F. Vilella, P. Alama, I. Moreno, M. Mignardi, A. Isakova, W. Pan, C. Simon, S. R. Quake, Single-cell transcriptomic atlas of the human endometrium during the menstrual cycle. *Nat. Med.* **26**, 1644–1653 (2020).
34. J. Min, N. Lu, S. Huang, X. Chai, S. Wang, L. Peng, J. Wang, Phenotype and biological characteristics of endometrial mesenchymal stem/stromal cells: A comparison between intrauterine adhesion patients and healthy women. *Am. J. Reprod. Immunol.* **85**, e13379 (2021).
35. E. S. Song, J. H. Park, S. S. Ha, P. H. Cha, J. T. Kang, C. Y. Park, K. Park, Novel corneal endothelial cell carrier couples a biodegradable polymer and a mesenchymal stem cell-derived extracellular matrix. *ACS Appl. Mater. Interfaces* **14**, 12116–12129 (2022).
36. C. Y. Gao, Z. H. Huang, W. Jing, P. F. Wei, L. Jin, X. H. Zhang, Q. Cai, X. L. Deng, X. P. Yang, Directing osteogenic differentiation of BMSCs by cell-secreted decellularized extracellular matrixes from different cell types. *J. Mater. Chem. B* **6**, 7471–7485 (2018).
37. H. Ragelle, A. Naba, B. L. Larson, F. Zhou, M. Prijić, C. A. Whittaker, A. del Rosario, R. Langer, R. O. Hynes, D. G. Anderson, Comprehensive proteomic characterization of stem cell-derived extracellular matrices. *Biomaterials* **128**, 147–159 (2017).
38. M. Li, T. Zhang, J. Jiang, Y. Mao, A. Zhang, J. Zhao, ECM coating modification generated by optimized decellularization process improves functional behavior of BMSCs. *Mater. Sci. Eng. C Mater. Biol. Appl.* **105**, 110039 (2019).
39. W. Liu, Y. Sun, X. Dong, Q. Yin, H. Zhu, S. Li, J. Zhou, C. Wang, Cell-derived extracellular matrix-coated silk fibroin scaffold for cardiogenesis of brown adipose stem cells through modulation of TGF-β pathway. *Regen. Biomater.* **7**, 403–412 (2020).
40. S. Abraham, M. J. Riggs, K. Nelson, V. Lee, R. R. Rao, Characterization of human fibroblast-derived extracellular matrix components for human pluripotent stem cell propagation. *Acta Biomater.* **6**, 4622–4633 (2010).
41. M. A. Dziasko, J. T. Daniels, Anatomical features and cell-cell interactions in the human limbal epithelial stem cell niche. *Ocul. Surf.* **14**, 322–330 (2016).
42. Y. C. Chee, J. Pahnke, R. Bunte, V. A. Adsool, B. Madan, D. M. Virshup, Intrinsic xenobiotic resistance of the intestinal stem cell niche. *Dev. Cell* **46**, 681–695.e5 (2018).
43. H. Lv, G. Zhao, P. Jiang, H. Wang, Z. Wang, S. Yao, Z. Zhou, L. Wang, D. Liu, W. Deng, J. Dai, Y. Hu, Deciphering the endometrial niche of human thin endometrium at single-cell resolution. *Proc. Natl. Acad. Sci. U.S.A.* **119**, e2115912119 (2022).
44. A. Naba, K. R. Clauser, S. Hoersch, H. Liu, S. A. Carr, R. O. Hynes, The matrisome: In silico definition and in vivo characterization by proteomics of normal and tumor extracellular matrices. *Mol. Cell. Proteomics* **11**, M111.014647 (2012).
45. S. M. Syed, M. Kumar, A. Ghosh, F. Tomasetig, A. Ali, R. M. Whan, D. Alterman, P. S. Tanwar, Endometrial axin2^{+} cells drive epithelial homeostasis, regeneration, and cancer following oncogenic transformation. *Cell Stem Cell* **26**, 64–80.e13 (2020).
46. S. Queckbörner, C. von Grothusen, N. R. Boggavarapu, R. M. Francis, L. C. Davies, K. Gemzell-Danielsson, Stromal heterogeneity in the human proliferative endometrium-a single-cell RNA sequencing study. *J. Pers. Med.* **11**, 448 (2021).
47. R. M. Gouveia, G. Lepert, S. Gupta, R. R. Mohan, C. Paterson, C. J. Connon, Assessment of corneal substrate biomechanics and its effect on epithelial stem cell maintenance and differentiation. *Nat. Commun.* **10**, 1496 (2019).
48. T. Nakajima, M. Kozuma, T. Hirasawa, Y. T. Matsunaga, Y. Tomooka, Extracellular matrix components and elasticity regulate mouse vaginal epithelial differentiation induced by mesenchymal cells. *Biol. Reprod.* **104**, 1239–1248 (2021).
49. B. Świerczek-Lasek, M. Keremidarska-Markova, K. Hristova-Panusheva, T. Vladkova, M. A. Ciemerych, K. Archacka, N. Krasteva, Polydimethylsiloxane materials with supraphysiological elasticity enable differentiation of myogenic cells. *J. Biomed. Mater. Res. A* **107**, 2619–2628 (2019).
50. Y. Wen, H. Yang, J. Wu, A. Wang, X. Chen, S. Hu, Y. Zhang, D. Bai, Z. Jin, COL4A2 in the tissue-specific extracellular matrix plays important role on osteogenic differentiation of periodontal ligament stem cells. *Theranostics* **9**, 4265–4286 (2019).
51. Y. Wang, S. Jin, D. Luo, D. He, C. Shi, L. Zhu, B. Guan, Z. Li, T. Zhang, Y. Zhou, C. Y. Wang, Y. Liu, Functional regeneration and repair of tendons using biomimetic scaffolds loaded with recombinant periostin. *Nat. Commun.* **12**, 1293 (2021).
52. H. Kuivaniemi, G. Tromp, Type III collagen (COL3A1): Gene and protein structure, tissue distribution, and associated diseases. *Gene* **707**, 151–171 (2019).
53. J. Bukowska, A. J. Ziecik, J. Laguna, B. Gawronska-Kozak, G. Bodek, The importance of the canonical Wnt signaling pathway in the porcine endometrial stromal stem/progenitor cells: Implications for regeneration. *Stem Cells Dev.* **24**, 2873–2885 (2015).
54. S. Yui, L. Azzolin, M. Maimets, M. T. Pedersen, R. P. Fordham, S. L. Hansen, H. L. Larsen, J. Guiu, M. R. P. Alves, C. F. Rundsten, J. V. Johansen, Y. Li, C. D. Madsen, T. Nakamura, M. Watanabe, O. H. Nielsen, P. J. Schweiger, S. Piccolo, K. B. Jensen, YAP/TAZ-dependent reprogramming of colonic epithelium links ECM remodeling to tissue regeneration. *Cell Stem Cell* **22**, 35–49.e7 (2018).
55. R. Pankov, K. M. Yamada, Fibronectin at a glance. *J. Cell Sci.* **115**, 3861–3863 (2002).
56. M. Jain, N. Dhanesha, P. Doddapattar, M. R. Chorawala, M. K. Nayak, A. Cornelissen, L. Guo, A. V. Finn, S. R. Lentz, A. K. Chauhan, Smooth muscle cell-specific fibronectin-EDA mediates phenotypic switching and neointimal hyperplasia. *J. Clin. Invest.* **130**, 295–314 (2020).
57. F. Klingberg, G. Chau, M. Walraven, S. Boo, A. Koehler, M. L. Chow, A. L. Olsen, M. Im, M. Lodyga, R. G. Wells, E. S. White, B. Hinz, The fibronectin ED-A domain enhances recruitment of latent TGF-β-binding protein-1 to the fibroblast matrix. *J. Cell Sci.* **131**, jcs201293 (2018).
58. A. Naba, K. R. Clauser, H. Ding, C. A. Whittaker, S. A. Carr, R. O. Hynes, The extracellular matrix: Tools and insights for the "omics" era. *Matrix Biol.* **49**, 10–24 (2016).
59. Y. Zhou, B. Zhou, L. Pache, M. Chang, A. H. Khodabakhshi, O. Tanaseichuk, C. Benner, S. K. Chanda, Metascape provides a biologist-oriented resource for the analysis of systems-level datasets. *Nat. Commun.* **10**, 1523 (2019).
60. A. Subramanian, P. Tamayo, V. K. Mootha, S. Mukherjee, B. L. Ebert, M. A. Gillette, A. Paulovich, S. L. Pomeroy, T. R. Golub, E. S. Lander, J. P. Mesirov, Gene set enrichment analysis: A knowledge-based approach for interpreting genome-wide expression profiles. *Proc. Natl. Acad. Sci. U.S.A.* **102**, 15545–15550 (2005).

Acknowledgments: We are grateful for Shanghai Applied Protein Technology Co. Ltd. for its technical support for proteomic analysis; R. Liu (Shimadzu) and R. Zheng (Shimadzu) for help regarding the AFM measurements; B. Su (Core Facilities of West China Hospital) for the help regarding the SEM measurements; and J.K. Pi (Core Facilities of West China Hospital), Y.J. Zhang (Core Facilities of West China Hospital), and F.F. Wang (Institute of hematology, West China Hospital) for help regarding cell culture and cytological identification. **Funding:** This study was supported by the National Natural Science Foundation of China (32171351), the Med-X Center for Materials, Sichuan University (MCM202104), the "1.3.5" Project for Disciplines of Excellence, West China Hospital, Sichuan University (ZYJC18002), and the Frontiers Medical Center, Tianfu Jincheng Laboratory Foundation (TFJC2023010002) to H.-q.X. **Author contributions:** Direction and supervision: H.-q.X. Conceptualization and experimental design: L.-m.Z. and L.-c.D. Experimental performance, data analysis, and data visualization: L.-m.Z., L.-c.D., X.-z.Z., Y.-l.J., Y.-x.L., C.-y.Z., and L.-p.H. Animal surgeries: J.L.-L., L.W., Y.-l.J., X.-x.L., Q.-y.Z., Y.L., and Y.Z. Pathology/histopathology assessment: R.W., Y.-t.S., W.-q.Z., and Q.-j.L. Writing-review and editing: H.-q.X., J.L.-L., and L.-m.Z.. All authors discussed and interpreted results throughout the duration of the investigation. **Competing interests:** H.-q.X., L.-m.Z., L.-c.D., and R.W. are inventors on patent application (ZL201811401674.7 and ZL201811400506.6) held by West China Hospital, Sichuan University that covers the preparation method and application of SPS and ECM-SPS. All other authors declare that they have no competing interests. **Data and materials availability:** The proteomic raw data were deposited in the ProteomeXchange database with access code PXD041467. All data needed to evaluate the conclusions in the paper are present in the paper and/or the Supplementary Materials.

Submitted 10 May 2023
Accepted 13 October 2023
Published 15 November 2023
10.1126/sciadv.adi6488